

The features of the Cosmic Web unveiled by the flip-flop field

Sergei F. Shandarin, ^{*} Mikhail V. Medvedev

Department of Physics and Astronomy, University of Kansas, Lawrence, KS 66045, USA

19 November 2021

ABSTRACT

Understanding of the observed structure in the universe can be reached only in the theoretical framework of dark matter. N-body simulations are indispensable for the analysis of the formation and evolution of the dark matter web. Two primary fields - density and velocity fields - are used in most of studies. However dark matter provides two additional fields which are unique for collisionless media only. These are the multi-stream field in Eulerian space and flip-flop field in Lagrangian space. The flip-flop field represents the number of sign reversals of an elementary volume of each collisionless fluid element. This field can be estimated by counting the sign reversals of the Jacobian at each particle at every time step of the simulation. The Jacobian is evaluated by numerical differentiation of the Lagrangian submanifold, i.e., the three-dimensional dark matter sheet in the six-dimensional space formed by three Lagrangian and three Eulerian coordinates. We present the results of the statistical study of the evolution of the flip-flop field from $z = 50$ to the present time $z = 0$. A number of statistical characteristics show that the pattern of the flip-flop field remains remarkably stable from $z \approx 30$ to the present time. As a result the flip-flop field evaluated at $z = 0$ stores a wealth of information about the dynamical history of the dark matter web. In particular one of the most intriguing properties of the flip-flop is a unique capability to preserve the information about the merging history of dark matter haloes.

Key words: methods: numerical – cosmology: theory – dark matter – large-scale structure of Universe

1 INTRODUCTION

Modern redshift surveys such as 2dF Galaxy Redshift Survey ¹ and the Sloan Digital Sky Survey ² as well as others reveal the wealth of structures in the spatial distribution of galaxies. A useful abstraction helping to comprehend the complexity of the structure has been provided by the skeleton of the web introduced by the adhesion approximation (Gurbatov et al. 1985, 1989, 2012; Hidding et al. 2012b,a). Its geometrical version designs a tiling of three-dimensional space by irregular three-dimensional tiles associated with voids. The faces of the tiles are associated with walls/pancakes, the edges – with filaments and the vertices – with the haloes. The geometrical model obviously highly simplifies the dark matter (hereafter DM) web especially its interior structure since it does not trace the details in the complex distribution of mass inside the walls, filaments and haloes. However the skeleton looks qualitatively quite realistic re-

vealing the multiscale nature of the web (Kofman et al. 1992). For instance, it indicated the presence of substructures in voids for the first time.

Historically, haloes have attracted the most of attention in theoretical studies of the large-scale structure formation. From the observational point of view, haloes are most closely related to galaxies, galaxy groups and clusters of galaxies, which provide the bulk of information about the structures in the universe. However, direct modeling of galaxy formation based on fundamental laws of physics is precluded by enormous complexity of the physical processes involved. In addition to the gravitational coupling with dark matter (hereafter DM) structure baryons participate in extremely complex hydrodynamical and thermal processes including star formation and the stellar wind feedback, shocks and supernovae explosions, gas accretion onto black holes in active galactic nuclei and the feedback via relativistic jets to name just some of them.

Hence various semi-empirical models of galaxy formation have been suggested, see e.g., Angulo et al. (2013) and references therein. In particular, it has been argued that galaxies are formed in the host DM haloes of corresponding

^{*} E-mail: sergei@ku.edu

¹ <http://msowwww.anu.edu.au/2dFGRS/>

² <http://www.sdss.org/>

masses. The DM haloes themselves are formed in a chain of mergers of smaller DM haloes which may start from tiny haloes of planet masses (Diemand et al. 2005). When two or more haloes merge their remnants may survive for a long time as subhaloes and/or streams within the resultant halo. Therefore, DM haloes are likely to have a nesting structure where each subhalo may include a number of even smaller subhaloes down to the smallest haloes allowed by the initial power spectrum (Diemand et al. 2005; Ghigna et al. 1998).

Dark matter structure results from the gravitational growth of the initial Gaussian perturbations of density. It is shaped by the nonlinear collisionless gravitational dynamics. Being very complex it is still considerably simpler than baryonic physics therefore it is more feasible to build the model of the DM web based on fundamental physical laws with a minimal number of heuristic assumptions. Cosmological N-body simulations play indispensable role in the studies of the DM web providing the most reliable data on the evolution of the web in highly nonlinear regime. However identifying the basic elements of the web (i.e. haloes, filaments, walls, and voids) represents a difficult problem even in pure DM N-body simulations where all dynamical information is readily available, see e.g., Colberg et al. (2008); Knebe et al. (2013); Cautun et al. (2014).

In early cosmological N-body simulations the haloes were loosely defined as compact concentrations of the simulation particles in configuration space. A particularly popular simple technique used for this purpose and called ‘friends of friends’ (FOF) algorithm was adopted from percolation analysis (Zeldovich et al. 1982; Shandarin 1983; Davis et al. 1985). According to this method one firstly finds all ‘friends’ of each particle by linking every particle in the simulation with all neighbors separated by less than a chosen distance – the linking length. Then applying the criterion: a friend of my friend is my friend, one can identify all groups of particles consisting of friends. Choosing a particular value of the linking length (often $\sim 20\%$ of the mean particle separation, Davis et al. (1985)) one can select a particular set of groups and call them haloes. A number of improved versions of FOF have been developed: Couchman & Carlberg (1992); Sugihara & Suto (1992); van Kampen (1995); Summers et al. (1995); Klypin et al. (1999); Okamoto & Habe (1999) just to mention a few. Other more sophisticated methods that identify both haloes and subhaloes have been suggested as well, for review see Knebe et al. (2013) and references therein. Some of them rely only on the particle positions, other also use the phase space information. The methods using only the configuration space information regardless of their sophistication may suffer from projection effect that causes dynamically distinct structures in phase space temporally to overlap in configuration space.

1.1 One-dimensional example

Let us consider a one dimensional example shown in Fig. 1. It shows the phase space of a halo simulated in a one-dimensional universe from some random but smooth initial condition. One can see a complicated substructure consisting of a number of subhaloes and streams shown in phase space by different colors. Using only the coordinates of particles means that the complicated phase space curve must be projected on the horizontal. It is obvious from the figure that

identifying individual subhaloes would be impossible even in a simple one-dimensional model. For instance the pair of subhaloes in red at the bottom of the figure is currently projected on the center of the halo and thus cannot be identified as separate subhaloes using particle coordinates only. But at a later time it will take place of the yellow subhalo on the left and thus may be identified as a separate pair of subhaloes. It becomes even more challenging in three-dimensional case, see e.g., Knebe et al. (2013); Hoffmann et al. (2014) and reference therein.

From Fig. 1 one can also see that a halo as well as subhaloes can be naturally defined as the regions in Eulerian space where the number of streams is greater than one (Shandarin et al. 2012; Ramachandra & Shandarin 2015, 2016). However, this approach also is not free of the contamination effects due to projection effects. Using all dynamical information available in phase space helps in solving this problem, however this is complicated by the fact that phase space is not a metric space, see e.g. Ascasibar & Binney (2005). Evaluating distances in phase space requires additional parameter with the dimensions of time. Unfortunately the time parameter is not universal for the whole halo. For illustration, consider again a simple example shown in Fig. 1. The spiraling time of two red subhaloes shown on the bottom of the figure is mostly determined by the density due to the subhaloes themselves $\tau_{\text{sh}} \propto \rho_{\text{sh}}^{-1/2}$ rather than by the total density dominated by the central part of the halo. This is because they spend a relatively short time in the spatial vicinity of the center. They live outside the central region of the halo the most of time since they move with lower speed there. In the outskirts of the main halo their dynamical time is determined primarily by their own densities. Thus finding the relevant local time requires identification of a subhalo in phase space which in turn requires the knowledge of the characteristic time of the same subhalo for making the corresponding patch of phase space metric.

One way overcoming this circular reasoning problem was suggest by Ascasibar & Binney (2005). It might be also possible to develop some iterative technique but we have tried a new completely different approach.

In order to outline the main idea of this new method we begin with a closer examination of the one-dimensional example introduced above. Let us follow along the phase space curve in the top left panel of Fig. 1 starting from the top point of the spiral on the left boundary of the box through the bottom point on the right boundary of the box. Along this path, the initial (Lagrangian) coordinates q_i of the particles, which are in essence their IDs and thus are immutable, increase monotonically while their final (Eulerian) coordinates x_i are not monotonic. This is also seen in the top right panel of Fig. 1 showing the Lagrangian submanifold of the halo which is the curve $x = x(q; t)$. In other words there are fluid elements with $x_{i+1} < x_i$ while $q_{i+1} > q_i$. Later on the Eulerian coordinates of these particles will swap again when they pass the caustic on the left hand side of the top left panel of Fig. 1. We will dub every swap of the Eulerian coordinates of the two neighboring (in Lagrangian space) particles on the curve as a flip-flop. The analog of this phenomenon in a multi-dimensional space is a formal change of the sign of the volume of a fluid element when it turns inside out. The volume of a fluid element is a continuous function of time, therefore between the states

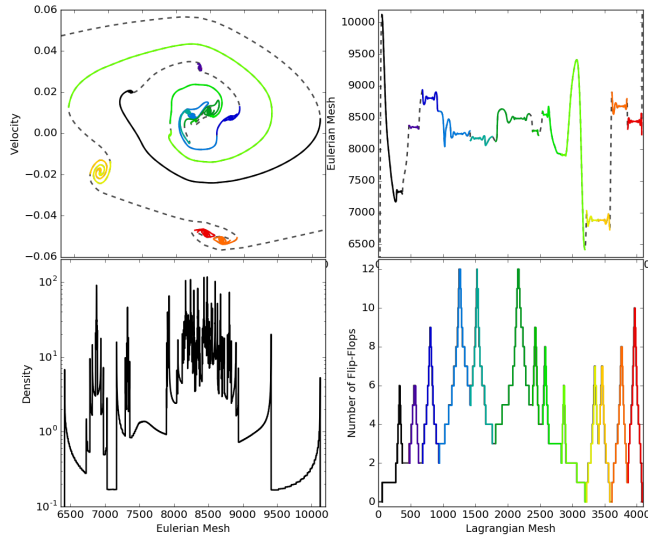


Figure 1. Illustration of a one-dimensional halo simulated from random but smooth initial condition. Top left panel: the phase space. Individual subhaloes are shown by different colors. Bottom left panel: density distribution in Eulerian space. Bottom right panel: the flip-flop field in Lagrangian space. Top right panel: Lagrangian submanifold $x = x(q)$. Colors in the panels on the right correspond to the colors in the top left panel. All panels correspond to the same instant of time.

of the volume with different signs it must be zero. At this moment in three-dimensional space it collapses into a piece of a two-dimensional surface called a caustic and its density becomes infinite. The caustic concept is of course a mathematical abstraction useful only when the discreteness effects are negligible.

The total number of flip-flops experienced by every fluid element by the time corresponding to the top left panel is shown in the bottom right panel of Fig. 1. We will refer to it as a flip-flop field. Colors show individual peaks of the flip-flop field in Lagrangian coordinates. The correspondence of the flip-flop peaks in Lagrangian space to individual subhaloes in the phase space shown in Fig. 1 is remarkable. Note that the tidal streams and haloes are also easily, unambiguously and robustly identified via the flip-flop field, cf. the bottom right and top left panels of Fig. 1. Using the flip-flop field in Lagrangian space is the key idea of a new approach to the analysis of DM haloes.

As far as we know the flip-flop phenomenon was firstly mentioned in cosmological context by Zel'dovich (1970). Later on it was used by Arnold et al. (1982) in the study of generic caustics and also discussed in the review by Shandarin & Zeldovich (1989). Recently the flip-flop phenomenon was used in the studies of a few specific problems Shandarin & Medvedev (2014). Here we briefly describe major differences between these studies and the approach discussed in this paper. Vogelsberger & White (2011) invoked it for the study of 'the properties of fine-grained phase-space streams and their associated caustics' by 'integrating the geodesic deviation equation' in cosmological N-body simulations. Although the counts of caustics was used for computing some one-point statistics the concept of a field in Lagrangian space was not even mentioned. Another method called "Origami"

was suggested in Neyrinck (2012) and Neyrinck et al. (2013) It was used for exploring the connectivity of streams in Lagrangian space. The authors used the results for approximating the boundaries of haloes, filaments and walls. In this approach a binary field with two values +1 and -1 corresponding to positive and negative parities of local Lagrangian volumes was introduced. The values of our flip-flop field can be any non-negative integer and its peaks play the key role in our study.

From dynamical point of view a subhalo can be described as a set of particles participating in oscillatory motions about some center which in turn orbits about the center of the halo or about the center of a larger subhalo. The both amplitudes of the oscillations of a subhalo in configuration and velocity spaces are significantly smaller than the corresponding sizes of the halo. The characteristic times of the oscillations are also significantly shorter than the corresponding time of the orbiting of the subhalo around the center of the halo. In a simple one-dimensional halo without subhaloes the number of flip-flops becomes a counter of full orbits: two flip-flops per a full orbit. It is worth mentioning that in such a halo the periods of orbits becomes shorter as the particle gets closer to the center because the mean density within smaller orbits is higher than that within the larger orbits since the period is proportional to $\langle \rho \rangle^{-1/2}$. The major goal of this paper is to investigate the properties of the flip-flop field in a three-dimensional N-body simulation and explore its potential usefulness for identifying the DM web, i.e., haloes, filaments, walls/pancakes, voids and their substructures.

1.2 Flip-flop field in two dimensions

Now we consider a two-dimensional example which may help to bridge the visualization gap between 1D in 3D.

The two-dimensional example is based on a simple N-body simulation in the EdS cosmological model with 2048² particles with equivalent mesh for computing CIC density and gravitational force via FFT. The initial power spectrum was $P \propto k^{-1}$ which corresponds to $P \propto k^{-2}$ in 3D in some important statistical aspects. The initial amplitude was normalized to give linear $\delta_{\text{rms}} = 1$ at the scale factor $a = 1$. The purpose of the simulation was to produce a single halo and evolve it for a long time in order to see how the structure originates and evolves in the flip-flop field. In particular how fast it gets erased or smeared by nonlinear processes or/and numerical noise.

Figure 2 shows four stages in the evolution at $a \approx 1.0, 2.3, 3.4$ and 58.7. Four panels on the left show the CIC density in Eulerian space and the panels on the right show the corresponding flip-flop fields in Lagrangian space. Although the colors look similar in all plots they have very different meanings. The density plots use the logarithmic scale with the same range in each plot $-1 < \log_{10} \rho < 3.5$ from gray to magenta. The flip-flop plots use linear scales with different ranges in all four panels: $0 < n_{\text{ff}} < n_{\text{ff,max}}$ where $n_{\text{ff,max}} = 10, 21, 25,$ and 86 from top to bottom respectively. The pattern in the flip-flop field evolves quite rapidly at the beginning of the non-linear stage. It needless to say that before shell crossing the field did not exist or was equal to zero at every point if it is more preferable. However, at the scale factor approximately between 3 and 4 the land-

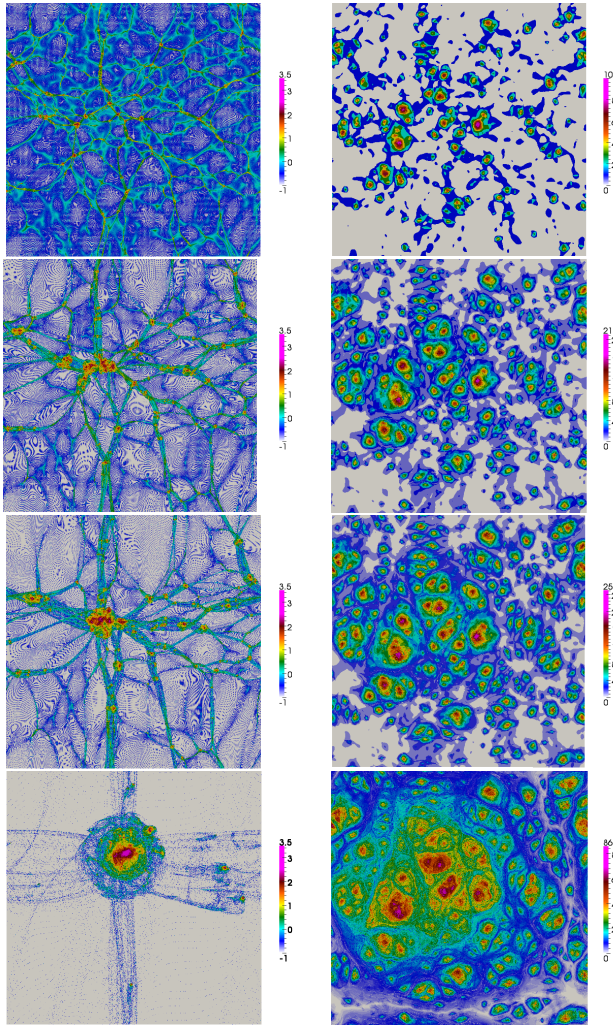


Figure 2. Evolution of structure in two-dimensional N-body simulation. Four stages are shown at $a \approx 1.0, 2.3, 3.4$ and 58.7 from top to bottom. The density perturbation linearly extrapolated would result in $\delta_{\text{rms}} = 1$ at $a = 1$. The CIC density fields in Eulerian space are shown in the left column. The corresponding flip-flop fields in Lagrangian space are shown on the right. The colors in the density plots are given on the logarithmic scale in the range $-1 < \log_{10} \rho < 3.5$ from gray to magenta. The colors in the flip-flop plots are given on different linear scales in the ranges $0 < n_{\text{ff}} < [10, 21, 25, 86]$ in four panels from top to bottom.

scape gets almost frozen. At later time the field continues to grow as the increasing range of the color legends show but the geometrical pattern evolves very little. For instance, all major peaks seen in the bottom panel corresponding to $a \approx 58.7$ could be easily identified in two middle panels corresponding to $a \approx 2.3$ and 3.4 . It is worth stressing that the major haloes shown in the corresponding density plots have not completed merging yet. The areas of gray and blue colors in flip-flop field may serve as visual indicators of the mass outside of the web. Here we do not show the results of the quantitative statistical analysis as they are similar to that in three-dimensional case presented in the following sections.

The paper is organized as follows. Section 2 explains the method in three dimensions in detail and Section 3 describes

the N-body simulation used in the study of the flip-flop field properties. After having presented the methodology in the previous sections we provide three-dimensional illustrations in Section 4. Then we discuss a number of statistical properties of the flip-flop field and in particular its peaks in Section 5. We also compare some properties of the flip-flop field with that of density and gravitational potential fields in Lagrangian space. In Section 6 we show that AGF haloes contain maxima of flip-flop fields. We present the results of the study of substructure evolution in the largest halo of the simulation. Section 8 is a short summary of the results.

2 METHOD

We propose a novel approach to the exploration of the DM web in cosmological N-body simulations. So far most of the studies used either the particles, or density field in Eulerian space, or the velocity of the particles or gravitational potential field or various combinations of the above quantities. We will use the field in Lagrangian space formed by the number of turns inside out experienced by each DM fluid particle which we call a flip-flop field $n_{\text{ff}}(\mathbf{q}; a(t))$. We estimate the number of flip flops experienced by each N-body particle by analyzing the mapping $\mathbf{x} = \mathbf{x}(\mathbf{q}; a(t))$ at chosen times characterized by the value of the scale factor $a(t)$ normalized to the present epoch $a(z = 0) = 1$. The particle coordinates \mathbf{x} and \mathbf{q} are in Eulerian and Lagrangian spaces respectively. The Lagrangian coordinates are the comoving positions of the particles on a regular grid corresponding to the unperturbed initial state. Assuming DM to be cold this mapping, referred to as a Lagrangian submanifold, is a three-dimensional sheet in the six-dimensional space (\mathbf{q}, \mathbf{x}) .

The method is based on a concept of a DM sheet $\mathbf{v} = \mathbf{v}(\mathbf{x}; t)$ in phase space successfully employed to improve accuracy of the estimates of the density, velocity and other parameters in standard cosmological N-body simulations (Shandarin et al. 2012; Abel et al. 2012). The major difference between this concept and the conventional one lies in a different interpretation of the role of the particles in the simulations. Namely how they represent the state and evolution of the continuous DM medium. In contrast to the common interpretation of particles as carriers of mass, the new approach treats them as massless markers of the vertices of a tessellation of the three-dimensional DM sheet in six-dimensional phase space. And the mass is assumed to be uniformly distributed inside each tetrahedra of the tessellation (Shandarin et al. 2012; Abel et al. 2012; Hahn & Angulo 2016). Once the tessellation is built in the initial state of the simulation, it remains intact through the entire evolution. This requirement results in a significant difference between this approach and Delaunay tessellation suggested in Schaap & van de Weygaert (2000) for estimating the density from particle distributions, where the tessellation must be built at each time.

The particles being the vertices of the tessellation tetrahedra describe all deformations occurred to the geometry of the tessellation. However it remains continuous in both six-dimensional phase space (\mathbf{x}, \mathbf{v}) due to the Liouville's theorem as long as the thermal velocities of the DM particles are vanishing. In particular, the variations of tetrahedra sizes and volumes result in the corresponding change of the tetra-

hedra densities. This property is especially valuable because it makes the tessellation self-adaptive to the growth of density perturbations with time.

The DM phase-space sheet cannot cross itself in the case of a continuous medium which is an excellent model for cold DM down to scales of the order of a characteristic DM particle separation. However the most of N-body simulations use particles which are more massive than physical DM particles by many orders of magnitude. Thus on scales smaller than the mass resolution scale the simulations are strongly affected by the discreteness effects which emerge at the centers of DM haloes. One of these effects is selfcrossing of the DM phase space sheet. However the Lagrangian submanifold $\mathbf{x} = \mathbf{x}(\mathbf{q}; a(t))$ in six-dimensional space never crosses itself.

Although both (\mathbf{x}, \mathbf{v}) – and (\mathbf{q}, \mathbf{x}) – spaces contain all the information about a dynamical system allowing to compute the whole evolution from \mathbf{q} to \mathbf{x} as well as from \mathbf{x} to \mathbf{q} (see e.g. Landau & Lifshitz 2008) they obviously have very different properties. For instance, an advantage of the former consists in ability to calculate the kinetic energy of the system while an advantage of the latter consists in being a *metric* space. Therefore the latter is superior to the former in the analysis of geometry of the structure. Moreover, the Lagrangian submanifold $\mathbf{x} = \mathbf{x}(\mathbf{q})$, is a single-valued function, unlike the phase space sheet $\mathbf{v} = \mathbf{v}(\mathbf{x})$ or $\mathbf{x} = \mathbf{x}(\mathbf{v})$ which are multivalued in a projection on arbitrary three-dimensional space formed by any three axes out of six available (\mathbf{x}, \mathbf{v}) in the non-linear regime after shell crossing.

Identifying flip-flop events in three dimensions can be done by computing the Jacobian $J(\mathbf{q}, t) = |\partial x_i / \partial q_j|$ on each particle at each time step. If the sign of the Jacobian changes, the number of flip-flops for the corresponding particles is increased by one. We show that the flip-flop field $n_{\text{ff}}(\mathbf{q}; a)$ at fixed a exhibits features in generic three-dimensional N-body simulation similar to those described in one-dimensional simulation. The Lagrangian submanifold technique was implemented in the publicly available cosmological TreePM/SPH code GADGET (Springel 2005) to compute the flip-flop field.

3 N-BODY SIMULATIONS

The initial conditions were generated with NGenIC code³ with the standard Λ CDM cosmology, $\Omega_m = 0.3$, $\Omega_\Lambda = 0.7$, $\Omega_b = 0$, $\sigma_8 = 0.9$, $h = 0.7$ and the initial redshift $z = 50$. A set of simulations were carried out with a box $1h^{-1}$ Mpc, $M_{\text{b, dm}} \approx 1.2 \times 10^{11} M_\odot$. For illustration purposes, we present two zoomed-in simulations with 128^3 , $m_{\text{part}} \approx 5.7 \times 10^4 M_\odot$ and 256^3 , $m_{\text{part}} \approx 7.1 \times 10^3 M_\odot$ DM particles in a box with the comoving size of $1h^{-1}$ Mpc with the force resolution of $1.5h^{-1}$ and $0.75h^{-1}$ kpc respectively. The chosen size of the box is obviously too small for the purpose of deriving statistically valid properties of the haloes. However the main purpose of this work is different, namely we would like to demonstrate that the flip-flop field of haloes in a highly nonlinear dynamic state retains rich information about the haloes and their substructures as well as about

³ see h-its.org

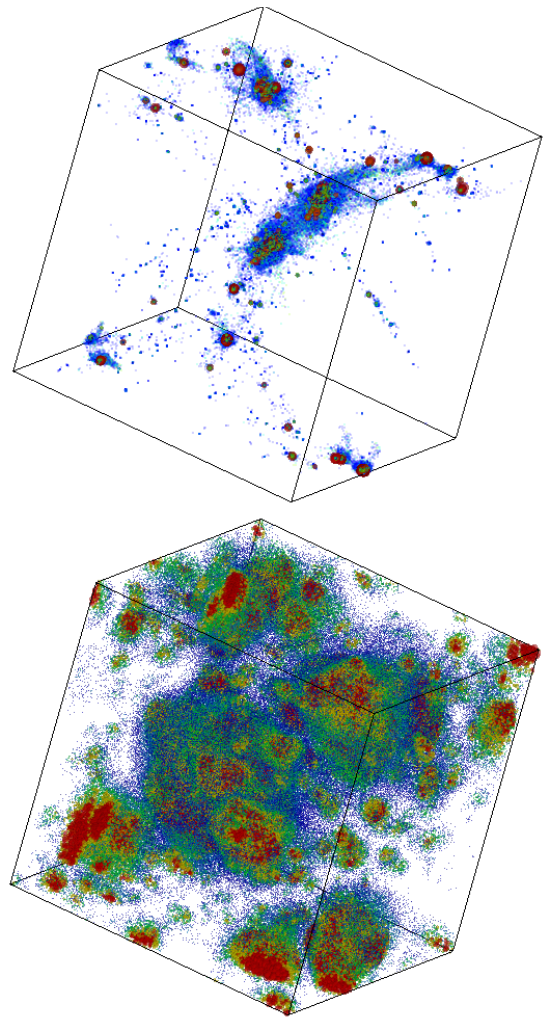


Figure 3. Top. The dot plot of a subset of particles with $n_{\text{ff}} \geq 6$ in the simulation of $1/h$ Mpc box in the Λ CDM cosmology at $z = 0$. The figure illustrates the densest regions of the simulation. Bottom. The subset of particles shown in the top panel is plotted in Lagrangian space. The sizes of dots are scaled by n_{ff} and the colors change with the growth of n_{ff} from blue to red.

their merging histories. We mark the epochs by the values of the scale factor a with $a = 1$ corresponding to the present time with $z = 0$. It is worth mentioning that the common parts of the initial Fourier spaces in two simulations have been generated with the same random numbers.

It is always useful to have a visual concept of any structure when its geometry or/and topology is discussed. The visualization of the major object in our analysis the submanifold $\mathbf{x} = \mathbf{x}(\mathbf{q}; a(t))$ in six-dimensional (\mathbf{q}, \mathbf{x}) – space is obviously out of question even in two dimensions. Its projection on \mathbf{x} – space is familiar in the form of ubiquitous dot plots illustrating the results of various N-body simulations. We are interested in visual illustration of the projections on \mathbf{q} – space which encounters additional problems compared to the visualization of \mathbf{x} – space outlined below.

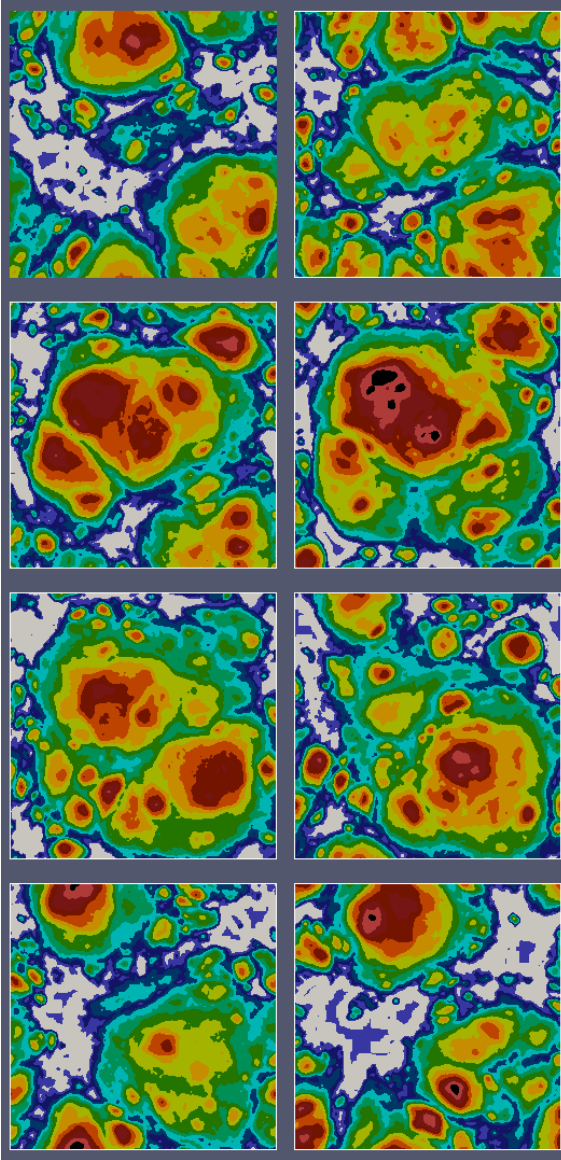


Figure 4. Eight panels show XZ – slices equally spaced along y – axis. Colors are as follows: $n_{\text{ff}} < 1$ – white and $n_{\text{ff}} > 250$ – black, and the range $1 \leq n_{\text{ff}} < 250$ is split in 15 hues from blue to brown in equal intervals of $\log(n_{\text{ff}})$.

4 VISUALIZATION OF FLIP-FLOP FIELD IN THREE DIMENSIONS

4.1 Entire simulation box

The top of Fig. 3 shows the map of the excursion set $n_{\text{ff}}(\mathbf{q}, z = 0) \geq 6$ in the entire simulation box to Eulerian space. The sizes and colors (from blue to red) of the particles represent the number of flip-flops. Boosting the sizes of less abundant particles with high flip-flop numbers allows to see them in crowded regions dominated by numerous particles with low flip-flop values.

Illustrating the flip-flop field in Lagrangian 3D space represents even more difficult problem than the cosmic web in Eulerian space. This is because the dense regions of the web occupy a small fraction of the volume in \mathbf{x} – space as can be seen in the top of Fig. 3. But the fraction of the volume

with $n_{\text{ff}} \geq 1$ – approximately corresponding to the web – occupies more than 90% of the volume in \mathbf{q} – space as the bottom of Fig. 3 demonstrates. It shows the dot plot of the corresponding flip-flop field in \mathbf{q} – space with the same color coding. One can see that the flip-flop field has a large number of distinct peaks occupying the most of Lagrangian space however it is not as detailed as in two-dimensional case (Fig. 2) because some of the distant peaks are hidden beneath the nearby structures in the projection on two-dimensional figure.

In order to reveal the much greater richness and complexity of the structure of subhaloes in the flip-flop field, we also plot a set of two-dimensional slices through Lagrangian box in Fig. 4. This figure shows eight XZ slices equally spaced along y -axis through the entire 256^3 simulation box. The sequence of slices is ordered from the top left to bottom right panels. In order to suppress numerical noise we smoothed n_{ff} field with gaussian filter with the size being equal to the separation of particles on the Lagrangian grid. The colors are explained in the caption. A complex hierarchy of n_{ff} peaks is revealed in considerably greater detail however at the cost of losing a three-dimensional perspective. Unfortunately, this is a typical trade of one for the other.

Figure 5 shows two panels from the right hand column of Fig. 4 supplemented by the corresponding plots over lines shown in the left hand panels of Fig. 5. Each panel on the right hand shows three curves: the green and blue curves correspond to the raw and filtered fields computed on the vertices, while the red curves show the number of flip-flops on the cubic cells. The flip-flop field on the cells (assumed to be uniform within each cell) equals the mean of the filtered field at the corresponding eight vertices. Thus the red curves display averaged values. Both filtering and averaging play noticeable role only in the vicinities of sharp maxima and narrow minima. This suggests that the numerical noise is not too bad. However, filtering makes the contours significantly smoother.

4.2 An example of substructure in the highest flip-flop peak

In this section we focus on the highest flip-flop peak ($\max(n_{\text{ff}}) = 616$ at $a = 1$) in a set of the peaks selected by the condition $n_{\text{ff}} \geq 20$. It corresponds to one of dynamically most evolved haloes. Figure 6 shows the three-dimensional structure of the peak in six panels starting with the contour at $n_{\text{ff}} = 20$ in the top left panel. In each of five remaining panels we plot two contours: one in gray color shows the same contour as in the top left panel and the other at steadily increasing levels $n_{\text{ff}} = 42, 67, 100, 130, 162$ respectively. One can clearly see a rich nesting structure of the peak.

5 STATISTICAL PROPERTIES OF THE FLIP-FLOP FIELD

First we briefly discuss some of global statistical properties of the flip-flop field in comparison with density and gravitational potential fields. There is a subtlety in such a comparison. We compute the flip-flop field on particles therefore it is a Lagrangian field. The density can also be

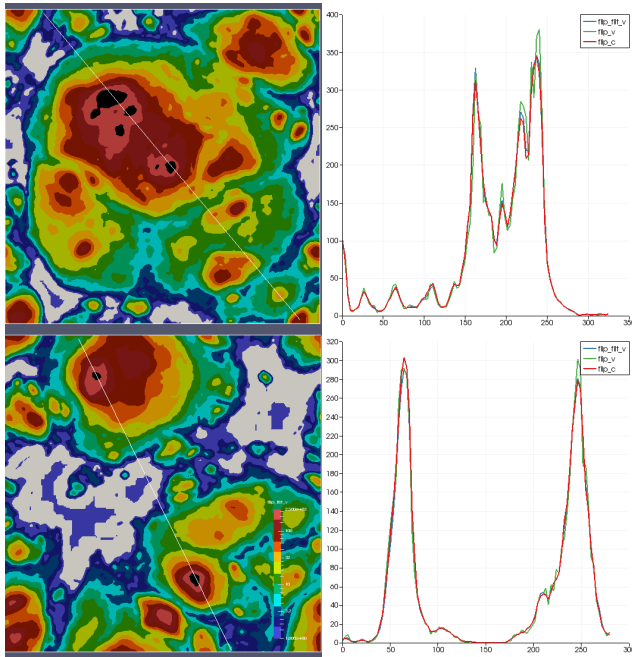


Figure 5. Two panels from the right column of Fig. 4 are shown along with plots over lines. The lines are shown in the left hand panels.

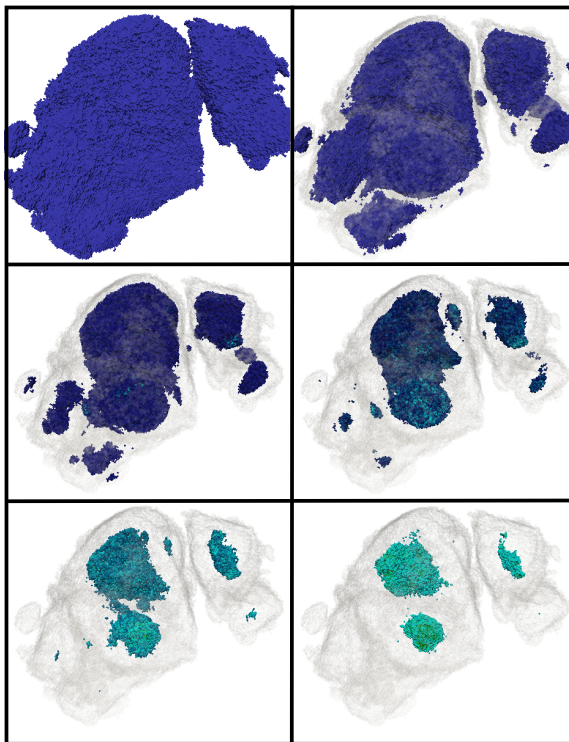


Figure 6. The substructure in the highest peak of the 256^3 simulation with $\max(n_{\text{ff}}) = 616$ is shown as a set of six isocontours in 3D. From top left panel to down right panel color contours are respectively: $n_{\text{ff}} = 20, 42, 67, 100, 130, 162$. Five panels show the gray shade of the contour at $n_{\text{ff}} = 20$ shown in the top left panel in blue.

computed on particles or in tetrahedra of the tessellation of the Lagrangian submanifold as described in Shandarin et al. (2012) and Abel et al. (2012), but this would be the density in separate streams not the total density in Eulerian space. Here we would like to compare the flip-flop field with commonly used density field computed in Eulerian space. However the interpolation of the Eulerian density to particles is not uniquely defined procedure. Since our simulations are done with GADGET code we use SPH densities and potentials computed on particles available in standard outputs of the code. We caution that other methods of computing density on particles may produce somewhat different results from reported here although we do not anticipate a substantial difference.

We start with making a list of obvious differences between three fields in question: (i) conceptually the number of flip-flops is a uniquely defined field in Lagrangian space but the SPH density or potential on particles in N-body simulations of a collisionless medium is only one of many feasible approximate maps of Eulerian fields to Lagrangian space, (ii) the flip-flop field is a discrete field with positive integral values while both density and potential are continuous fields apart from the discreteness related to the grid, (iii) both the flip-flop and density fields are positively defined while potential can be both positive and negative, (iv) the number of flip-flops monotonically grows with time at every particle while both the density and potential do not because some particles can move back and forth between high and low density environments as well between regions with high and low potentials.

5.1 Cumulative probability functions

Figure 7 shows the fractions of particles with densities above the threshold ρ_{th} in the range of $0.001 \geq \rho_{\text{th}} \geq 15$ and the fractions of particles with the number of flip-flops above the threshold n_{th} in the range $1 \geq n_{\text{th}} \geq 50$ in the top and bottom panels respectively. The ranges correspond approximately 90% of lowest values of the fields in both plots. The plots of the cpf showing the highest 1% of the values are shown in Fig. 8. The cpf is shown for both 128^3 and 256^3 simulations.

The figures demonstrate that the cpf of the flip-flop field is considerably more regular function of the cosmological epoch and the size of the simulation than the density in Lagrangian space. The flip-flop cpf monotonically increases with time and with the mass resolution of the simulation. The density cpf seems do not show clear dependence on either the size of the grid or the epoch.

5.2 The growth of the web mass

The fraction of mass experienced the strongest non-linear event – flip-flop – monotonically increases with time. The slope of the power spectrum of the linear density perturbations in the range from the Nyquist wavelength $L_{\text{Ny}} \approx 16 h^{-1}$ kpc or $\approx 8 h^{-1}$ kpc in 128^3 or 256^3 simulation respectively to the size of the simulation box is quite steep. Therefore the fraction of mass reached a strong non-linear regime when a fluid element experiences a flip-flops grow very fast. The blue curves in Fig. 9 and 10 show the frac-

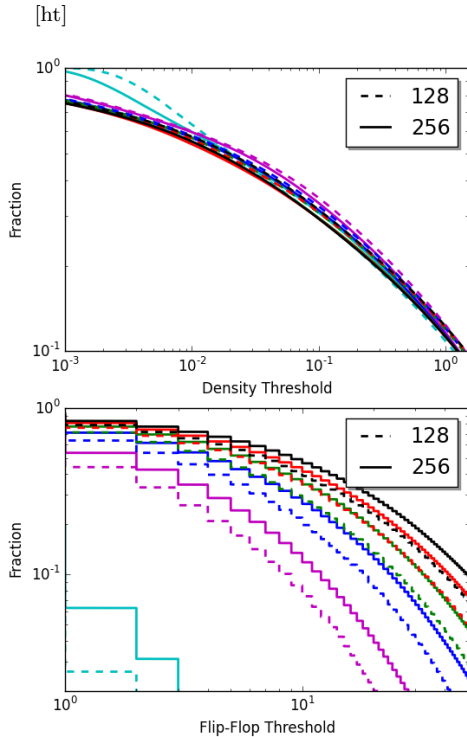


Figure 7. The cumulative probability functions of the lowest 90% of density (top) and flip-flop (bottom) fields are shown at six epochs: $a = 0.026, 0.058, 0.129, 0.242, 0.493, 1.000$ in 128^3 and 256^3 simulations. Colors in the order of epochs are: cyan, magenta, blue, green, red and black.

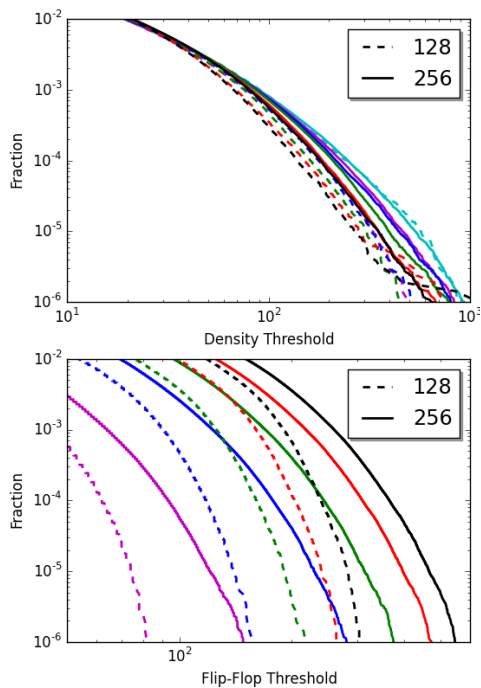


Figure 8. Same as Fig. 7 except that these are the cpfs of the highest one percent of the values of the fields are shown.

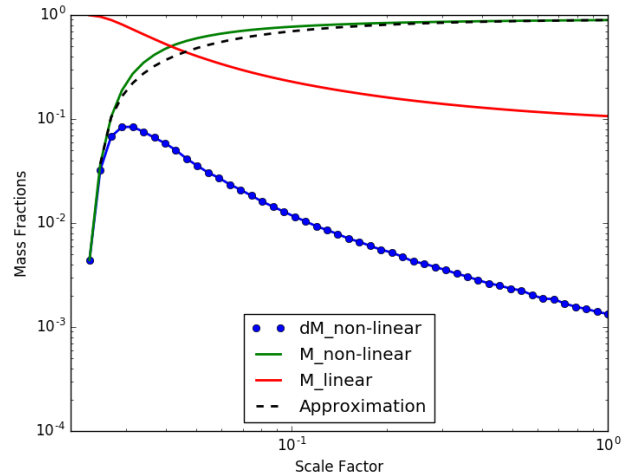


Figure 9. 128^3 simulation. A blue line with dots shows the fractions of mass experienced the first flip-flop between $(i-1)$ -th and i -th outputs of the N-body code as a function of a_i . The green curve shows the accumulation of mass experienced at least one flip-flop by a_i while the red curve demonstrates the mass fraction which have not experienced flip-flops at all by a_i . The dashed line in black shows a crude analytical approximation to the green line.

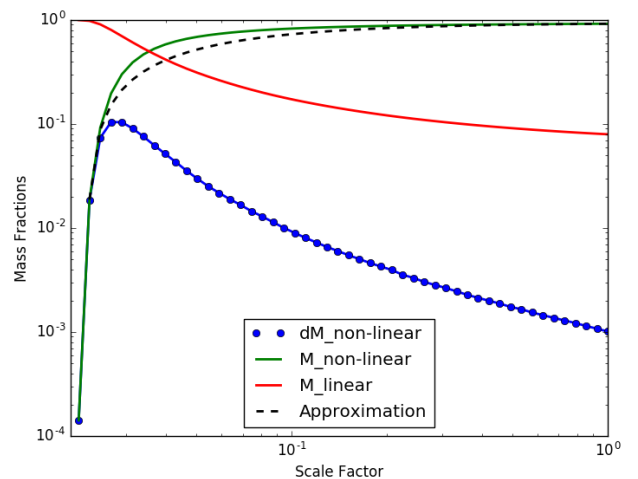


Figure 10. 256^3 simulation. Notations are the same as in Fig. 9

tions of mass experienced the first flip-flop between the output times equally spaced on the $\log_{10}(a)$ scale from approximately 0.023 to 1. The green lines show the growth of the mass fraction experienced at least one flip-flop by a_i while the red lines show the decrease of the mass fraction that did not experience even a single flip-flop. After reaching about a third of the total mass at $a \approx 0.03$ the growth of the mass in the non-linear regime is steadily reducing reaching about 0.1% by the present time ($a = 1$). The total mass in the particles never experienced flip-flops has dropped to about 10% or 8% in the 128^3 or 256^3 simulations respectively. The black dashed line is a crude analytical approximation of the growth of the mass fraction reached non-linearity by a function with two free parameters

$$f(a) = C_1 - \frac{C_2}{a}.$$

The parameters are chosen to make the approximation curve to pass through the second and last points of the green curve obtained in the N-body simulations. The approximation obviously is far from perfect and is not intended for further use. It still may be useful because it demonstrates a very fast growth of the mass in the dark matter web, which is probably faster than exponential rate between $a = 0.023$ and $a = 0.03$. In the 128^3 simulation $C_i = (0.022, 0.92)$ and in the 256^3 simulation the are $C_i = (0.021, 0.94)$ showing that the difference between two simulation is noticeable but quite small.

5.3 Correlation properties

5.3.1 Correlations between the pairs of different fields at the same epoch

It is expected that the density, potential and flip-flop fields correlate with each other since the higher densities and higher numbers of flip-flops tend to be more frequent in the regions of negative potential. In order to quantify these anticipations we evaluate the correlation coefficients of the fields in question at a number of epochs in both 128^3 and 256^3 simulations. Figure 11 shows each correlation coefficient as a function of a scale factor. They exhibit a remarkably weak evolution if any with time. The highest correlation is between the potential and flip-flop fields, while the lowest is between potential and density fields. Both become weaker with the growth of the mass resolution while the correlation coefficient of the density and flip-flop fields seems to be very similar in both simulations. The correlations between the density and flip-flop fields is intermediate for these simulations and do not show any dependence on the size of the simulation. Its magnitude being around 0.45 suggests that the fields seem to resemble each other but they are not very similar. Both dependences on the size of the simulation looks natural. Adding small scale power to the initial perturbations in the 256^3 simulation results in reducing the scale of the both density and flip-flop fields without a significant effect on the scale of the potential.

5.3.2 Correlations between the pairs of the same field taken at different epochs

Here we present the correlation coefficient of the same field taken at two different epochs: $\text{corcoef}[f(a_i), f(a_{\text{ref}})]$ where $f = [\rho, \phi, n_{\text{ff}}]$ i.e., it is either density or potential or flip-flop field. We selected two reference epochs: $a_{\text{ref}1} = 1$ and $a_{\text{ref}0.1} = 0.1$. In both cases we compute the correlation coefficients with all previous stages $a_i < a_{\text{ref}}$. In order to emphasize how close to unity the correlation coefficient of the flip-flop field is we plot $\log(1 - \text{corcoef}(f_i, f_k))$ instead of $\log(\text{corcoef}(f_i, f_k))$ in Fig. 12.

It is no surprise that three fields correlate stronger when two epochs get closer to each other. However the strength of the correlation as well as dependence on the epoch a_i are substantially different between all three fields. The density correlation coefficient shown in red is the lowest and the most stably growing from about 0.2 at the largest separation of the epochs to about 0.5 for the closest epochs. There is practically no difference between 128^3 and 256^3 simulations and barely noticeable difference between two reference

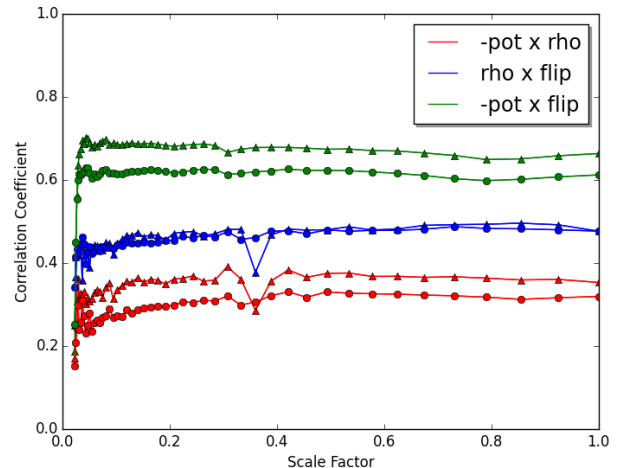


Figure 11. Correlation coefficients of all pairs of three Lagrangian fields in Lagrangian space: negative potential (- pot), density (rho) and flip-flop (flip) as a function of the scale factor. Triangles and circles correspond to the simulations with 128^3 and 256^3 particles respectively.

epochs $a = 1$ and $a = 0.1$. The potential correlation coefficient shown in blue is significantly higher with the range from about 0.75 to 0.95 with distinct difference between two reference epochs $a = 0.1$ and $a = 1$.

The overall highest correlation coefficient and the greatest difference between two reference epochs is displayed by the flip-flop field. Although it is similar to the density correlation coefficient at the largest separation of the epochs it grows very quickly above 0.9 at $a_i \approx 0.03$ and then above 0.99 at $a_i \approx 0.05$ and at $a_i \approx 0.2$ for the reference epochs $a = 0.1$ and $a = 1$ respectively. Such a small difference between the correlation coefficient and unity suggests that the difference of the fields at the corresponding epochs is mostly due to a constant factor. It means that the geometry of the flip-flop field does not evolve much after some epoch which means in turn that the peak structure in the flip-flop field keeps the record of the formation of the haloes even after they experienced mergers with other haloes.

5.4 Comparison of the flip-flop, density and potential fields in Lagrangian space

We computed the ratios of a field at chosen epoch a_i to it at a reference epoch $a_{\text{ref}} > a_i$: $R_{i,\text{ref}}^{(F)} = F(\mathbf{q}, a_i)/F(\mathbf{q}, a_{\text{ref}})$, where F is either the flip-flop or density or potential field and a_{ref} is either 0.1 or 1. Then we estimated the mean, median and standard deviations of the ratio fields. Figure 13 shows the results for all three fields at 47 scale factors in the range from 0.02 to 0.92 when the reference field was chosen at $a = 1$ and at 18 scale factors in the range from 0.02 to 0.087 when the reference field was chosen at $a = 0.1$. The mean and std values are shown in black and red colors respectively in three panels: flip-flop field - in the top, potential - in the middle, and density - in the bottom panels of Fig. 13. The median values of $R_{i,\text{ref}}^{(F)}$ are shown by green dots.

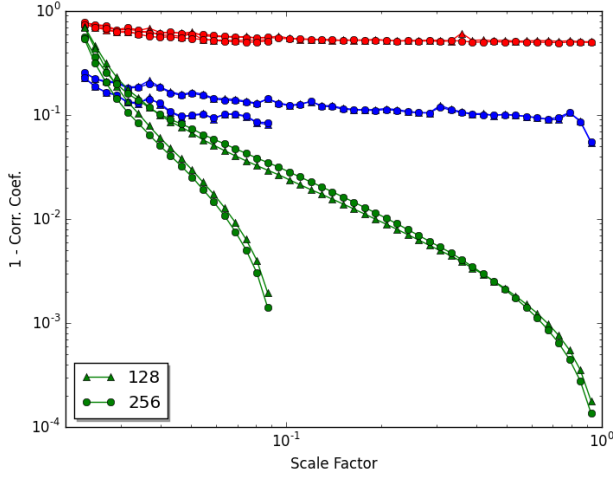


Figure 12. Correlation coefficient of the density $\xi_{\rho\rho}$ (red), potential $\xi_{\varphi\varphi}$ (blue) and flip-flop $\xi_{ff,ff}$ fields at $a = 1$ (long curves) and $a = 0.1$ (short curves) with corresponding fields at all previous stages. In order to see how close to unity $\xi_{ff,ff}$ is we plot the logarithm of its difference from unity. The curves are shown for both $N_p = 128$ (triangles) and 256 (circles) simulations.

5.4.1 Flip-flop field (top panel of Fig. 13)

For the majority of the epochs a_i the values of $\sigma(R_{i,\text{ref}}^{(\text{ff})})$ is significantly smaller than the mean and median values which are practically the same: $\sigma(R_{i,\text{ref}}^{(\text{ff})}) \ll \text{mean}(R_{i,\text{ref}}^{(\text{ff})}) = \text{median}(R_{i,\text{ref}}^{(\text{ff})})$. It demonstrates that the flip-flop field grows in very orderly manner with stochastic effects being quite small.

5.4.2 Potential field (middle panel of Fig. 13)

The difference between $\text{mean}(R_{i,\text{ref}}^{(\varphi)})$ and $\text{median}(R_{i,\text{ref}}^{(\varphi)})$ are more distinct at large separations of the epochs and significantly diminishes as the epochs get closer. The most conspicuous difference of $R_{i,\text{ref}}^{(\varphi)}$ from $R_{i,\text{ref}}^{(\text{ff})}$ is a large value of std at all epochs $\sigma(R_{i,\text{ref}}^{(\varphi)}) \gg \text{mean}(R_{i,\text{ref}}^{(\varphi)}) \approx \text{median}(R_{i,\text{ref}}^{(\varphi)})$ with the lowest value of about twice of the mean at the smallest separation from $a = 1$.

5.4.3 Density field (bottom panel of Fig. 13)

The evolution of $R_{i,\text{ref}}^{(\rho)}$ is essentially stochastic: $\sigma(R_{i,\text{ref}}^{(\rho)}) \sim 100 \times \text{mean}(R_{i,\text{ref}}^{(\rho)})$ and $\sigma(R_{i,\text{ref}}^{(\rho)}) \sim 1000 \times \text{median}(R_{i,\text{ref}}^{(\rho)})$ making both rather useless.

Summarizing Section 6.3 we would like to stress the qualitative difference between evolutions of the flip-flop and SPH density and gravitational potential fields evaluated on particles. The flip-flop evolves in a remarkably orderly manner with mean and median of the ratios $n_{\text{ff}}(\mathbf{q}, a_i)/n_{\text{ff}}(\mathbf{q}, a_{\text{ref}})$ being almost exactly equal and std being much smaller. It is a strong evidence that the geometry of the flip-flop field in Lagrangian space evolves very little. On the contrary the evolution of the potential and especially density field is almost stochastic: while the both the mean and median of the ratios of the both fields monotonically increase with time the standard deviations are considerably greater at all epochs making the mean and median useless.

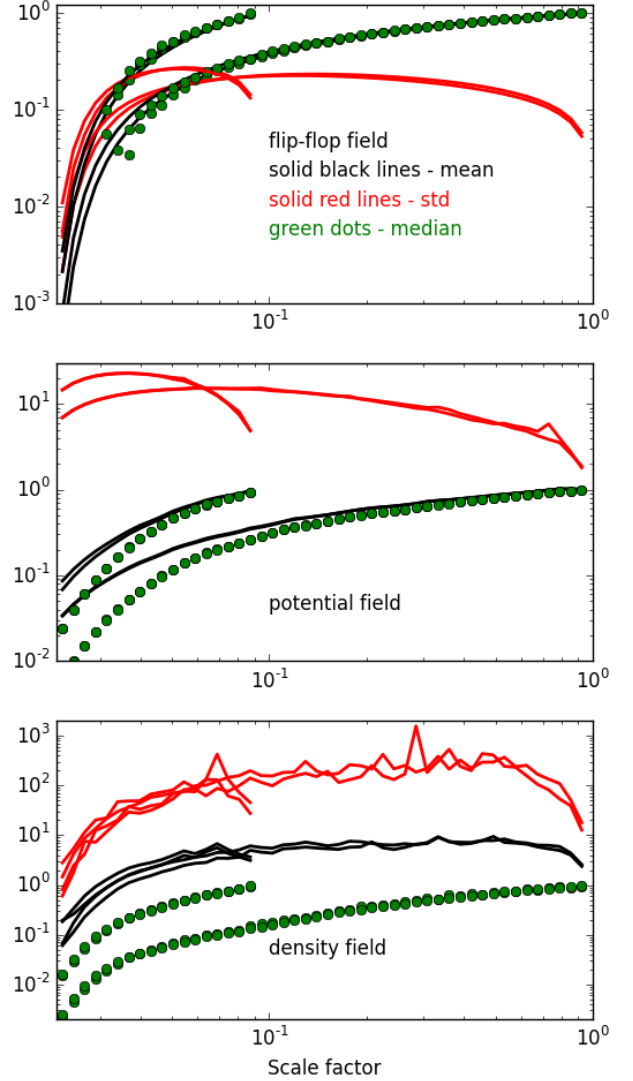


Figure 13. The mean, std and median of the ratios of the field at the scale factors shown on the horizontal to the same field at the reference scale factor. Two sets of curves correspond to two reference scale factors $a = 0.1$ (short curves) and $a = 1$ (long curves). The curves corresponding to 128^3 and 256^3 simulations noticeably different only for mean and std values of the density field shown in the bottom panel.

5.5 A unique feature of the evolution of the flip-flop field

Discussing a simple one-dimensional halo in Introduction we argued that the closer the orbit of a fluid element to the center of the halo the shorter its characteristic time. It means that the earlier the fluid element collapsed for the first time the greater its counts of flip-flops at later epochs. A similar rule is also valid in generic haloes with substructures in three-dimensions although it is not exact but valid in statistical sense as we describe below. Figure 14 provides a quantitative illustration of this assertion.

For the plot we selected and binned particles according to their gains in flip-flops counts $\Delta n_{\text{ff}} = n_{\text{ff}}(a_{i+1}) - n_{\text{ff}}(a_i)$ where a_i mark the output stages of the 256^3 simulation.

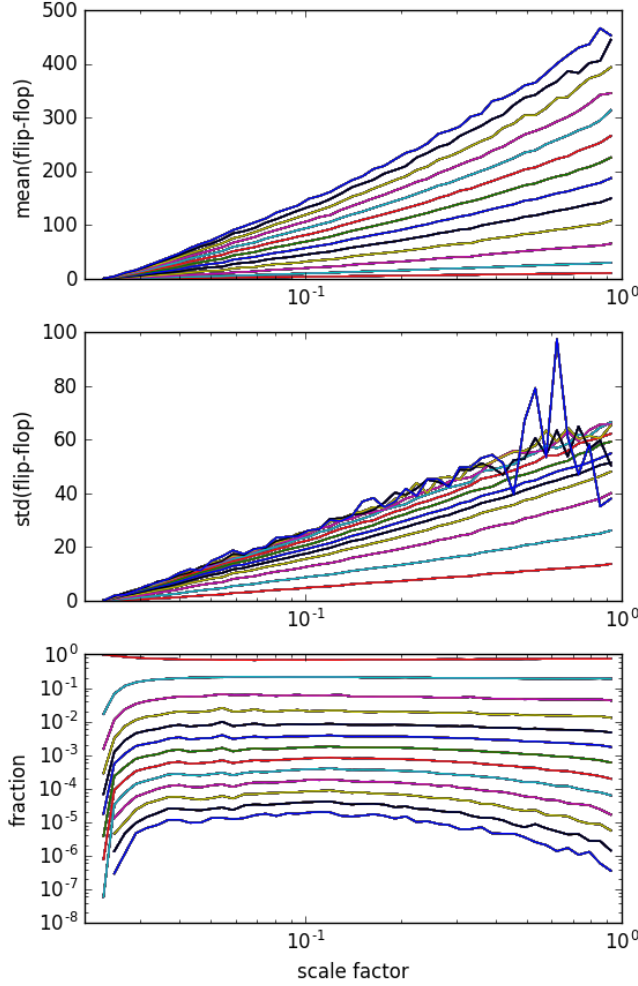


Figure 14. Conditional statistics of the flip-flop field as a function of the scale factor. The particles are binned according to the change of the number of flip-flops between the outputs $\Delta n_{\text{ff}} = n_{\text{ff}}(a_{i+1}) - n_{\text{ff}}(a_i)$. The curves are in the range $0 \leq \Delta n_{\text{ff}} \leq 12$ from the bottom to top in top two panels and in the reverse order in the bottom panel. The panels show the mean, std and fraction of the particles in each bin from top to bottom

Then we computed the mean number of flip-flops $n_{\text{ff}}(a_i)$, standard deviation $\sigma(n_{\text{ff}}(a_i))$ and the fractions of the particles in thirteen bins with $0 \leq \Delta n_{\text{ff}} \leq 12$. Thirteen lines in the top panel show $\text{mean}[n_{\text{ff}}(a_i)]$ for each bin in ascending order of Δn_{ff} from the bottom to top. The middle panel shows $\sigma(n_{\text{ff}}(a_i))$ for all bins, the order of bins is same as in the top panel⁴. The bottom panel shows the fraction of particles in every bin. Obviously the lines in this panel are in the reversed order of two top panels: the largest fraction of particles gets zero raise at all times (red line).

Although the particles do not always stay in the same bin their mobility between bins is rather limited. The bins reasonably well separated as $\sigma(n_{\text{ff}}(a_i))$ in the middle panel show. In addition the particles in the higher bin have on average higher $\text{mean}[n_{\text{ff}}(a_i)]$ and higher raise Δn_{ff} . Thus the

⁴ Large fluctuations of $\sigma(n_{\text{ff}}(a_i))$ for a couple of the highest bins is caused by very limited statistics as the bottom panel shows.

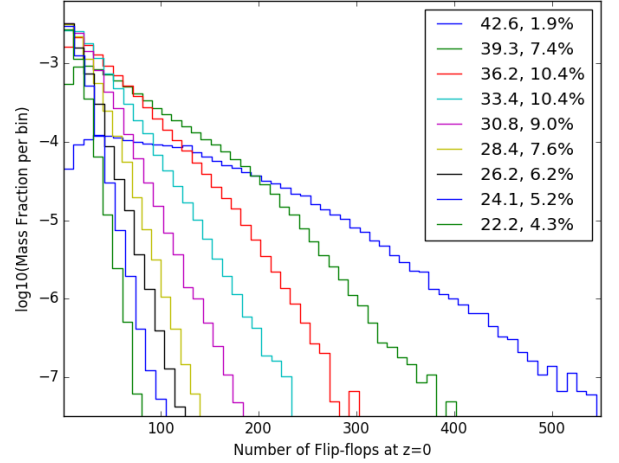


Figure 15. The logarithm of the fraction of mass in bins with the number of flip-flops at $z = 0$ shown on the horizontal. Nine curves correspond to the particles experienced first flip-flopping before redshift shown in the first column of the legend except those experienced flip-flopping before the previous redshift. For example, the second (green) curve from the right corresponds to the particles that did not experience a single flip-flop before $z = 42.6$ but experienced some by $z = 39.3$. The second column in the legend shows the total fractions of the mass in the particles satisfying the above criterion.

particles that gained superiority in the number of flip-flops at early nonlinear stages on average remain among the leaders at later times. Therefore we conclude that the contrast between peaks of different heights and valleys in the flip-flop landscape on average does not diminish with time. However in N-body simulations some saddle points in the n_{ff} landscape may disappear due to discreteness effect and other sources of numerical noise.

Figure 15 provides an additional evidence for the conclusion of the previous paragraph. It shows the histogram of mass fractions in the bins of the final counts of flip-flops at $z = 0$ in nine sets of particles. The first set comprising about 1.9% of all particles are particles experienced first flip-flops at $z > 42.6$. The corresponding histogram is shown by blue curve on the right demonstrates the distribution of the flip-flop counts at $z = 0$. The next histogram in green shows the final distribution of the numbers of flip-flops on particles that entered the nonlinearity, i.e. experienced flip-flops, at $39.3 < z < 42.6$, comprising 7.4% of all mass so forth until the group of particles experienced first flip-flop at $22.2 < z < 24.1$. The corresponding redshifts and amounts are shown in the figure legend in two columns. The figure is clearly demonstrates that at $z = 0$ the high counts of flip-flops, say $n_{\text{ff}} > 50$, are dominated by the particles experienced first flip-flops at $z > 36.2$. They make less than 20% of the total mass or less than 22% of all particles experienced at least one flip-flop as Fig. 15 shows. These particles obviously make the tips of the highest peaks of the flip-flop field.

5.6 The number of peaks

Now we will turn to the issue of the number of peaks in the flip-flop field. It is worth stressing that here we do not mean

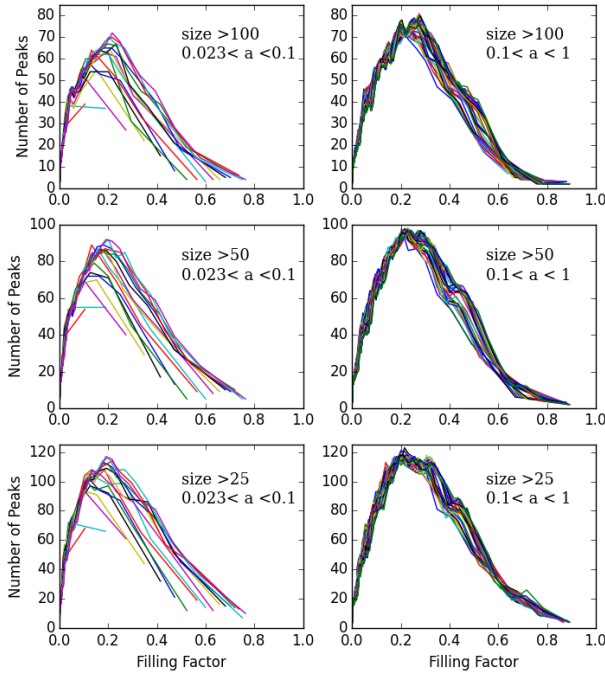


Figure 16. Number of peaks as a function of filling factor is plotted for every output of the simulation with 128^3 particles. The counts for outputs at early stages $a < 0.1$ are shown on the left and the rest are shown on the right. The counts are made for three thresholds of the size as shown in the panels.

the points of maxima of n_{ff} in Lagrangian space but rather the regions of the field with the number of flip-flops above a certain level. More exactly we will look at the evolution of the excursion set in the flip-flop field at all fifty output epochs. The peaks and their structures represent the major interest because they are associated with the haloes and subhaloes.

Figures 16 and 17 show the number of peaks as a function of the filling factor at every output epoch in the 128^3 and 256^3 N-body simulations. We count peaks with three different sizes: > 100 , > 50 and > 25 particles. The left panels show earlier stages $a < 0.1$ characterized by relatively fast evolution and the right panels show later stages with $0.1 \leq a \leq 1$ when the evolution is considerably slower. The number of peaks increases with the growth of the filling factor as the threshold is decreasing and reaches a broad maximum around $FF \approx 0.2$. Then at greater filling factors many peaks begin to merge with each other and therefore their number decreases.

It is remarkable that at $a > 0.1$ the curves corresponding to different scale factors a are packed quite tightly forming a relatively narrow strip. This behavior is quite different from that at earlier stages $a < 0.1$. There is no much difference between the 128^3 and 256^3 simulations apart from the number of peaks, which is expected. Generally it is in agreement with the results described in previous sections and confirms that the geometry of the flip-flop landscape does not evolve much at $a > 0.1$.

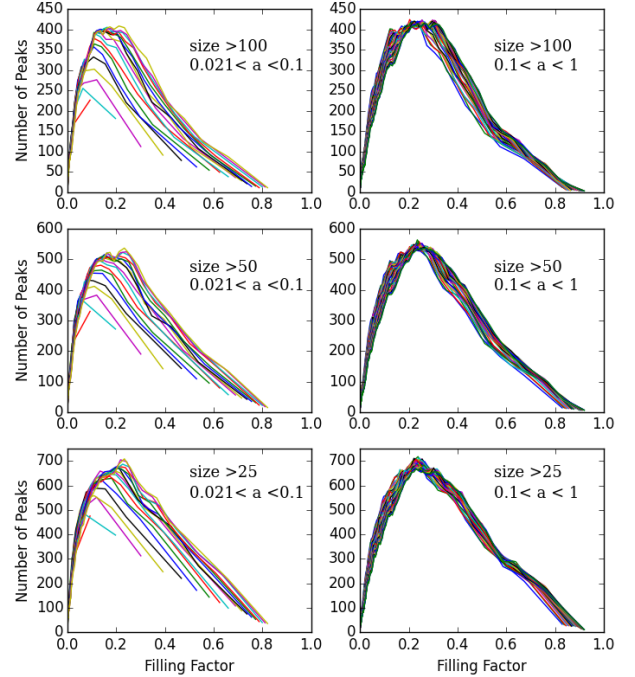


Figure 17. Same as in Fig. 16 but for the simulate with 256^3 particles.

6 COMPARISON WITH AHF HALOES

6.1 Illustration

As we indicated in Introduction there are many different methods and techniques used to identify and study haloes, in particular DM haloes. We compare the positions of the maxima of the flip-flop field a publicly available halo finder called Amiga Halo Finder or AHF (Knollmann & Knebe 2009; Gill et al. 2004) for comparison of some flip-flop peak properties with AHF haloes. We are arguing that the peaks of the flip-flop field computed in Lagrangian space are directly related with the DM haloes. If it is true then the maxima of the flip-flop field must be inside of the AHF haloes. In order check this we find the maxima of the flip-flop field in Lagrangian space and map them in Eulerian space. Figure 18 shows two orthogonal projections of one of the largest haloes found by the AHF in our simulation. The halo is shown as a sphere of the virial radius. It also shows the subhaloes with more than a hundred particles. The centers of the virial spheres are shown as white dots. The particles with the maxima of the flip-flop field are shown by small colorful spheres where both the radii and colors reflect the magnitude of the flip-flop maxima. Colors from dark blue to red correspond to the ascending order of the heights of the maxima. Generally both the colorful spheres and white dots are clearly seen in one or the other projection. However in a few cases the spheres obscure the centers of the virial spheres in both projections. The largest red sphere shows the particle with the maximum value of flip-flops corresponding to the virial center of the halo itself.

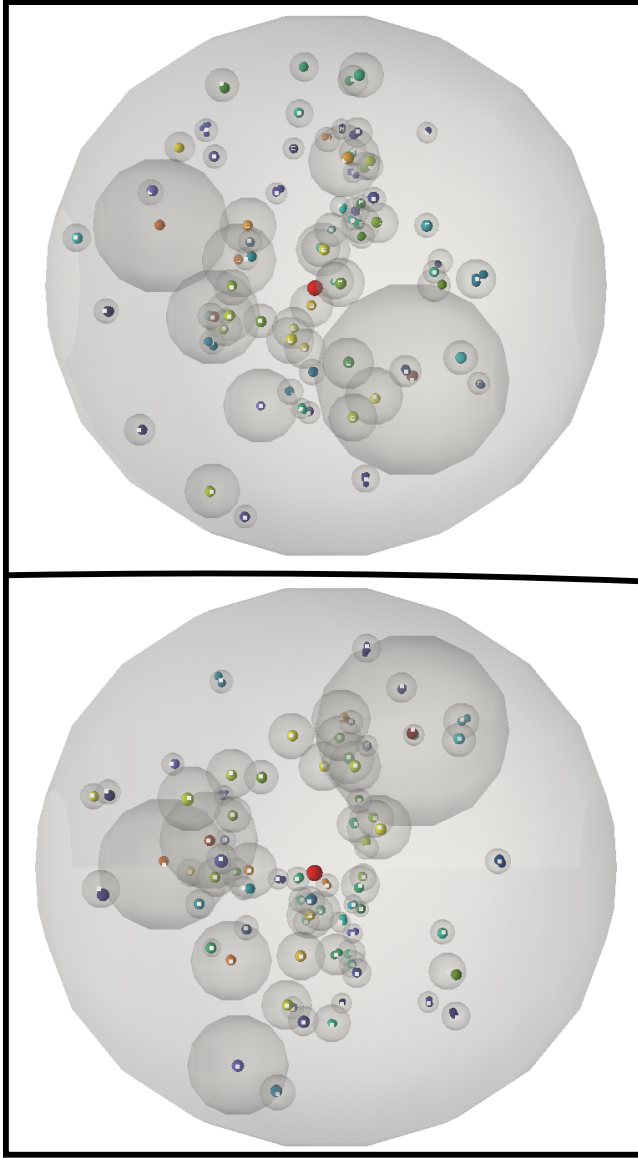


Figure 18. Two mutually orthogonal views of one of the largest halo along with its subhaloes in the simulation found by the AMF code. The haloes are represented by the spheres of the virial radii. Small colored spheres mark the particles with the maximum value of the flip-flop field and white dots show the centers of the sphere, some of which may be obscured by the respective colored spheres.

6.2 Statistics

In order to quantitatively address the question of how close are the maxima of the flip-flop field to the virial centers of the AHF haloes we computed the cumulative probability function of the ratios R_{\max}/R_{vir} for haloes or subhaloes with more than thirty particles. First we selected all the particles with the largest value of flip-flop, i.e. the global maximum in each set of particles comprising a halo or subhalo identified by the AFH algorithm. In most of haloes it was just a single particle, however since the number of flip-flops is integral on rare occasions – mostly in haloes with fewer than a hundred particles – more than one particle had the largest count of flip-flops. Then for each particle with the maximal count of flip-flops we computed the distance from the virial

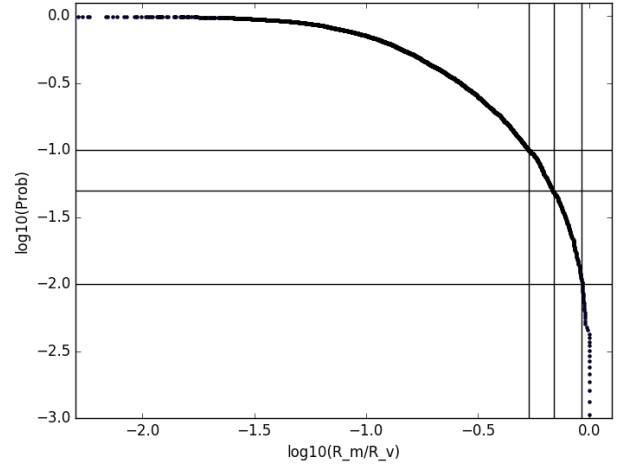


Figure 19. Cumulative probability function of the ratio R_{\max}/R_{vir} . Three horizontal lines show 1, 5 and 10% levels and the vertical lines show the corresponding values of R_{\max}/R_{vir} which are 0.92, 0.69 and 0.54 respectively, i.e., for example, in 90% of haloes the distances of the flip-flop maxima are less than 0.54 of the virial radius.

center of the halo or subhalo. The cumulative probability function of the ratios R_{\max}/R_{vir} is displayed in Fig. 19. For convenience we show three horizontal lines marking 1, 5 and 10% of particles with highest values of the ratio R_{\max}/R_{vir} . The vertical lines show the corresponding values of the ratio. Thus $R_{\max}/R_{\text{vir}} < 0.54, 0.69, 0.92$ in 90%, 95% and 99% of the haloes respectively.

In order to show how the positions of the maxima of flip-flops, their values and masses of haloes correlate we provide the scatter plots of three pairs of these parameters in Fig. 20. The top panel shows the correlation of the maxima with the number of particles in the halo. For the haloes with more than about 200 particles the tendency that the larger the halo the higher maximum of the flip-flop in the halo is unambiguously clear. The tendency of the ratio R_{\max}/R_{vir} to decrease with the growth of the halo mass is also quite clear shown in the middle panel. The bottom panel exhibits similar tendency with the growth of the flip-flop maximum of the halo at $ff_{\max} \gtrsim 20$, which qualitatively follows from the correlations displayed in the top and middle panels. For haloes with $N_p \lesssim 200$ or/and $ff_{\max} \lesssim 20$ these correlations are not observed.

The horizontal lines in the middle and bottom panels correspond to the vertical lines in Fig. 19. Although they show that the largest ratios of R_{\max}/R_{vir} are characteristic for small haloes with low maxima of flip-flops but the most of them have a clear maximum of the flip-flop field within a sphere centered on the virial center and the radius less than about a half of the virial radius. It is worth stressing that the haloes with fewer than a hundred particles are probably seriously affected by numerical noise in our simulations.

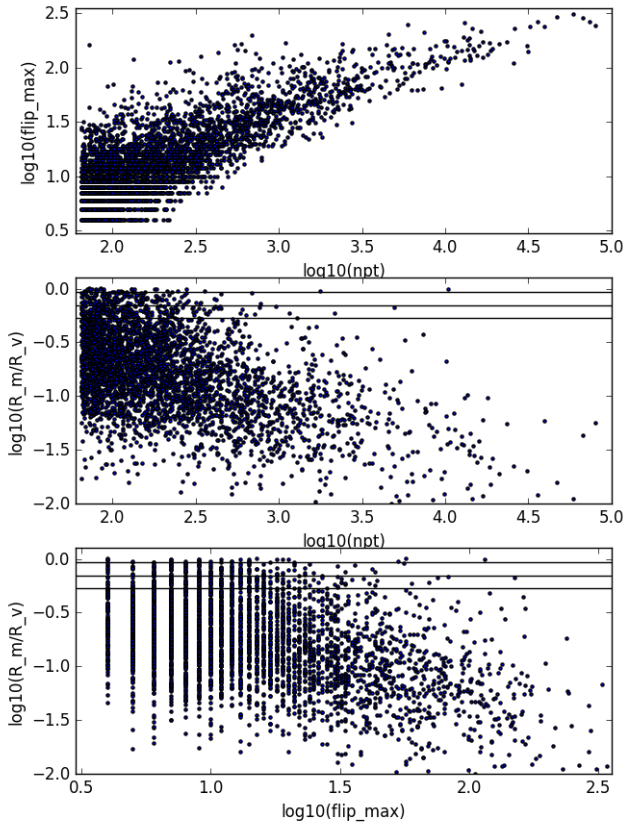


Figure 20. Two top panels show the flip-flop maxima and the ratio R_{\max}/R_{vir} respectively vs the number of particles in selected AMF haloes. The bottom panel shows the ratio R_{\max}/R_{vir} vs the maximum of the flip-flop field in the haloes. Horizontal lines in two lower panels correspond to the vertical lines in Fig. 19, i.e. $R_{\max}/R_{\text{vir}} = 0.92, 0.69, 0.54$

7 THE EVOLUTION OF THE HIGHEST FLIP-FLOP PEAK

7.1 Statistics of subpeaks in one of the largest peaks

First we look at the dependence of the number of subpeaks defined as peaks within a parent peak. The parent peak is selected as a compact region at some threshold $n_{p,\text{th}}$. Then we continuously elevate the threshold n_{th} up to the highest maximum within the peak and identify distinct subpeaks with sizes greater than selected threshold at each level n_{th} . We repeat this procedure three times for three size thresholds: 100, 50 and 25 particles. The bottom panel of Fig. 21 shows this dependence in the 256^3 simulation. Three lines show the effect of the size threshold as indicated by the legend. For comparison and as an illustration of the effect of the small scale cutoff in the power spectrum of the initial density perturbations the top panel shows the substructure in the 128^3 simulation⁵. As expected the number of substructures increases with the size of the simulation box and

⁵ We are reminding that the common part of the Fourier amplitudes was the same in both simulations

Table 1. Number of particles in substructures shown in Fig. 22

flip-flop threshold	N_1	N_2	N_3	N_4	N_5	N_6	N_7
100	206670						
150	61960	17035	513	308	265		
240	8698	3960	211				
270	4363	1474	753	521			
300	1976	416	405	381	286	267	178

Table 2. Approximate masses of substructures shown in Fig. 22 in units of $10^6 M_{\odot}$

flip-flop threshold	M_1	M_2	M_3	M_4	M_5	M_6	M_7
100	1464.						
150	439.	121.	3.63	2.18	1.87		
240	61.6	28.1	1.50				
270	30.9	10.4	5.34	3.70			
300	14.0	2.94	2.87	2.70	2.03	1.89	1.26

decreases with the growth of the size threshold. This is in a qualitative agreement with Fig. 16 and 17.

7.2 Selection of subpeaks

In order to make an unambiguous case we consider only substructures selected by two conditions: one by their sizes in Lagrangian space that can be quantified by the number of particles $n_{\text{ff}} \geq n_{\text{ff,thr}} = 100$ and the other by their heights $n_{\text{p}} \geq n_{\text{p,th}} = 100$. Therefore we identify individual substructure within the parent peak at four thresholds: $n_{\text{ff}} = 150, 240, 270,$ and 300 . The choice is based on the red curve in the bottom panel of Fig. 21.

The flip-flop subpeaks in Lagrangian space are displayed in Fig. 22. The parent peak in three-dimensional space represents a nesting structure resembling a generalized Russian doll or ‘matreshka’-doll. Combining all five levels of this substructure in one plot significantly obscures the complex geometrical pattern of the largest peak. Therefore we show the substructure in four steps each of which displays only two levels of the nesting structure: the low level of substructure is shown as gray surfaces and the higher level as color surfaces. Surfaces are the convex hulls of the peaks. Color scheme is same in every step: the colors (blue, magenta, cyan, green, yellow, and red) correspond to the sizes/masses of subpeaks in descending order. Thus the top left portion of Fig. 22 shows levels (1,2), top right – levels (2,3), bottom left – levels (3,4), and bottom right - levels (4,5). The sizes and masses of the peaks at every level are given in Tables 1 and 2.

It is worth stressing that Fig. 22 does not show the entire substructure of the largest peak. Four thresholds were selected on the basis of the red line in the bottom panel of Fig. 21 as a few representative examples of substructure. The three-dimensional illustration is shown in Fig. 22 and their parameters are given in Table 1 and 2 which display the number of particles and the masses respectively

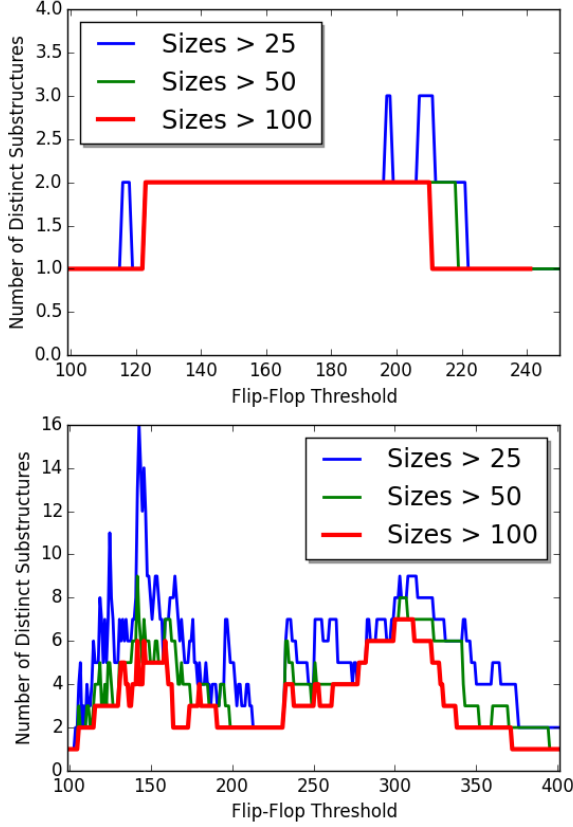


Figure 21. Number of subpeaks within the largest flip-flop peak as a function of the threshold. The top and bottom panels correspond to the 128^3 and 256^3 simulations respectively. The lines of different colors show the dependence on the size threshold as indicated by the legend.

7.3 Illustration of the evolution of the largest flip-flop peak

In this section we will closely follow the evolution of seven highest peaks selected by the condition $n_{\text{ff}} \geq 300$ at $z = 0$. We demonstrate that these peaks of the flip-flop field become small individual haloes at early times. Then we show how they merge with each other in a hierarchical process of assembling the parent halo. Finally we illustrate how they evolve after they all reside in the central region of the cloud formed by the particles of the parent peak selected by the condition $n_{\text{ff}} \geq 100$. It is worth stressing that only particles corresponding to the bottom right panel of Fig. 22 retain their colors in the plots described in this section (i.e. Figs. 23, 24 and 25). All the rest particles are in black. According to Table 1 the total number of particles in these peaks is only 3,909 which makes less than 2% of the parent peak comprised of 206,670 particles. Thus we consider a tiny fraction of the collapsed region within a gray surface in the top left corner of Fig. 22, or more accurately as a cloud of particles in the top left panel of Fig. 23⁶. It is worth emphasizing that it makes only the central part of the largest halo. The

⁶ For the purpose of better visualization the boundary surfaces of the peaks in Fig. 22 are approximated by the convex hulls. No calculation used this approximation.

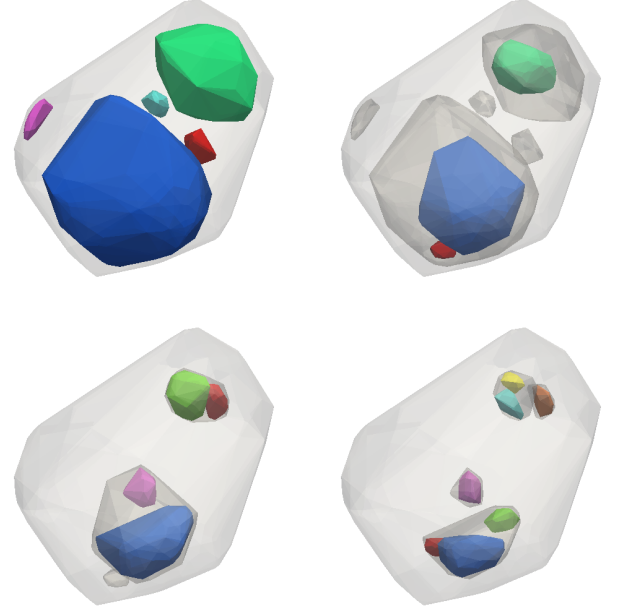


Figure 22. Contours of the flip-flop field show five levels of hierarchical structure of the largest flip-flop peak in the 256^3 simulation. The top left panel shows the convex hull of the peak identified as a connected region with $n_{\text{ff}} \geq 100$ in gray and five distinct substructures at $n_{\text{ff}} \geq 150$ in color. In the remaining three panels the contour $n_{\text{ff}} = 100$ is displayed in light gray. The top right panel displays the convex hulls at $n_{\text{ff}} \geq 150$ in light pink that are shown in the previous panel in color and three substructures at $n_{\text{ff}} \geq 240$ in color. The bottom subplots show three contours at $n_{\text{ff}} = 240$ in light pink and four at $n_{\text{ff}} = 270$ in color on the left and four contours at $n_{\text{ff}} = 270$ in light pink and seven at $n_{\text{ff}} = 300$ in color. Colors in order blue, dark cyan, green, light brown, and dark brown correspond to the mass of the substructures in descending order .

whole halo is even more massive since there are particles with $n_{\text{ff}} < 100$ in the region in question.

We concentrate on this small set of particles because they reside in the highest density environment and thus have experienced the most vigorous dynamical evolution. The major question we are interested in is what is the final state of particles in the selected seven peaks of the flip-flop field. In particular is it feasible to identify them as distinct structures in Eulerian space at $z = 0$.

Figures 23, 24 and 25 show a sequence of dot plots illustrating the evolution of selected particles from $z = 50$ to $z = 0$ or respectively from $a = 0.02$ to $a = 1$. Each figure shows the structure formed by these particles at four redshifts indicated in the captions. It is no surprise that the colorful particles find themselves in the central parts of the cloud of black particles and thus become obscured very quickly. In order to see the structures formed by them more clearly each of four panels in every figure consists of two parts: all particles are plotted on the left hand side and only colorful particles are shown on the right hand side. Please note that the orientation in Fig. 22 is different from that in Figs. 23, 24 and 25 where it is the same. The orientations in Lagrangian and Eulerian spaces were chosen with the goal of minimizing obscuration due to projection.

The top panel of Fig. 23 shows the initial state at $z =$

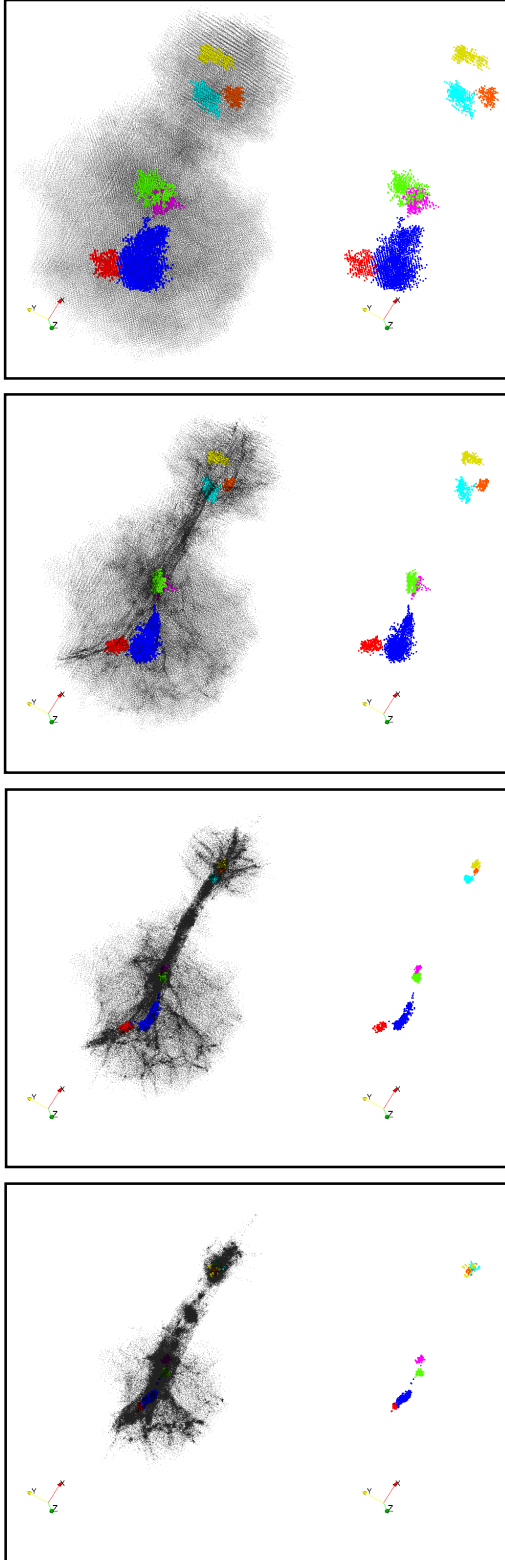


Figure 23. The figure illustrates the evolution of the whole halo and its substructure shown in color in the bottom right panel of Fig. 22. The plots on the left show all particles in the halo in gray and the particles of the substructure are shown in color on both sides. The stages from the top to bottom corresponds to $z = 50, 42.6, 39.3, 36.2$ or respectively $a = 0.020, 0.023, 0.025, 0.027$. All plots have the same scale.

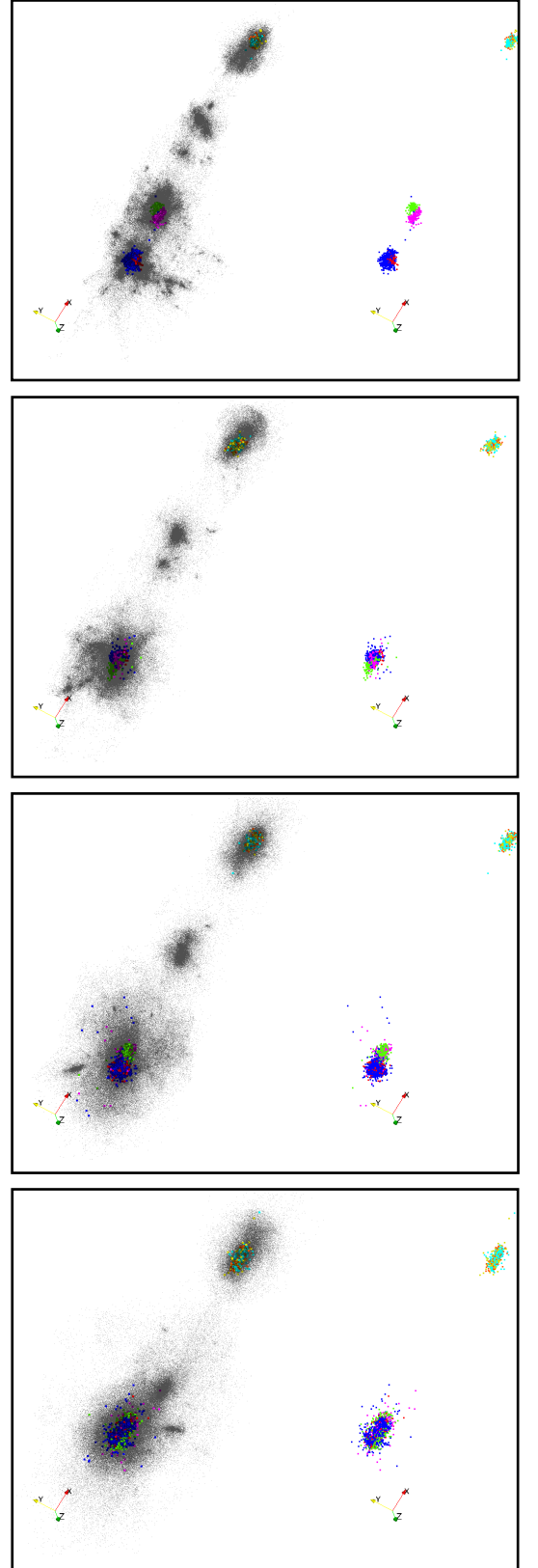


Figure 24. Same as Fig. 23 except the stages are $z = 33.4, 30.8, 28.4, 26.2$ or respectively $a = 0.029, 0.031, 0.034, 0.037$. In order to improve the visibility of subhaloes the plots are progressively zoomed in with time.

50. The shape of the cloud of black particles in Fig. 23 is more accurate than the gray surface in the top left corner of Fig. 22 because the latter is the convex hull of the cloud in Fig. 23. Except for this particular case other peaks are of remarkably convex shapes and thus approximating them by convex hulls in Fig. 22 is quite accurate. Convex hulls require fewer surface elements and thus improve visibility of nesting surfaces depicted in Fig. 22.

The top panel in Fig. 23 shows Lagrangian space. The second from the top panel shows the first output ($z = 42.6$) when the flip-flop field on some particles differs from zero. By $z = 39.3$ shown in the second from the bottom panel of Fig. 23 the colorful particles collapsed in small haloes incorporated into a complicated filament formed by black particles.

The top panel of Fig. 24 shows that at $z = 33.4$ seven colorful haloes merged into three larger haloes approximately corresponding to the bottom left panel in Fig. 22. One can see four or even five haloes on the left hand side of this panel but only three of them contain colorful particles. The flip-flop peaks corresponding to two smaller haloes without colorful particles emerged from peaks lower than $n_{\text{ff}} = 300$ on which the colorful particles have been selected. The rest panels of Fig. 24 illustrate the hierarchical process of merging of colorful particles. The bottom panel of Fig. 24 shows that all colorful particles merged in two haloes. It is worth noting that the colorful particles reside inside bigger haloes of black particles.

Finally the top panel of Fig. 25 displays the state when all colorful particles merged into a single halo at $z = 24.1$. The remaining three panels show three states at $z = 9.58, 3.82$ and finally at $z = 0$. The cloud of colorful particles is well mixed and remains intact after $z \approx 10$.

In order to see the central part of the halo it has been zoomed in and the colorful particles are plotted with greater sizes than black particles. In addition the opacity of black particles has been reduced. Without this trickery the colorful particles were hardly being seen at all.

The outputs of the simulation are equally spaced in logarithm of the scale factor a . Starting from the second from top panel in Fig. 23 until the top panel of Fig. 25 every output is displayed. Two middle panels of Fig. 25 show just two states in a long evolution from $z = 24.1$ shown at the top to $z = 0$ shown at the bottom. There are probably two remarkable features in this evolution. First, the orientation of both the central part of the halo depicted by the colorful particles and fifty times more massive part of the halo shown by black particles substantially and synchronously have changed their orientation. This obviously happened because they are only small central parts of a much more massive halo experienced considerable accretion of mass. Second, the final state shown by colored particles looks like a dynamically relaxed configuration with all seven subpeaks marked by different colors well mixed. Nevertheless they are easily identified as distinct peaks of the flip-flop field $n_{\text{ff}}(\mathbf{q}, z = 0)$ in Fig. 22.

8 SUMMARY

We explored the properties of flip-flop field in the N-body simulations designed to simulate the formation of DM haloes at very early stage of the evolution of the universe. We con-

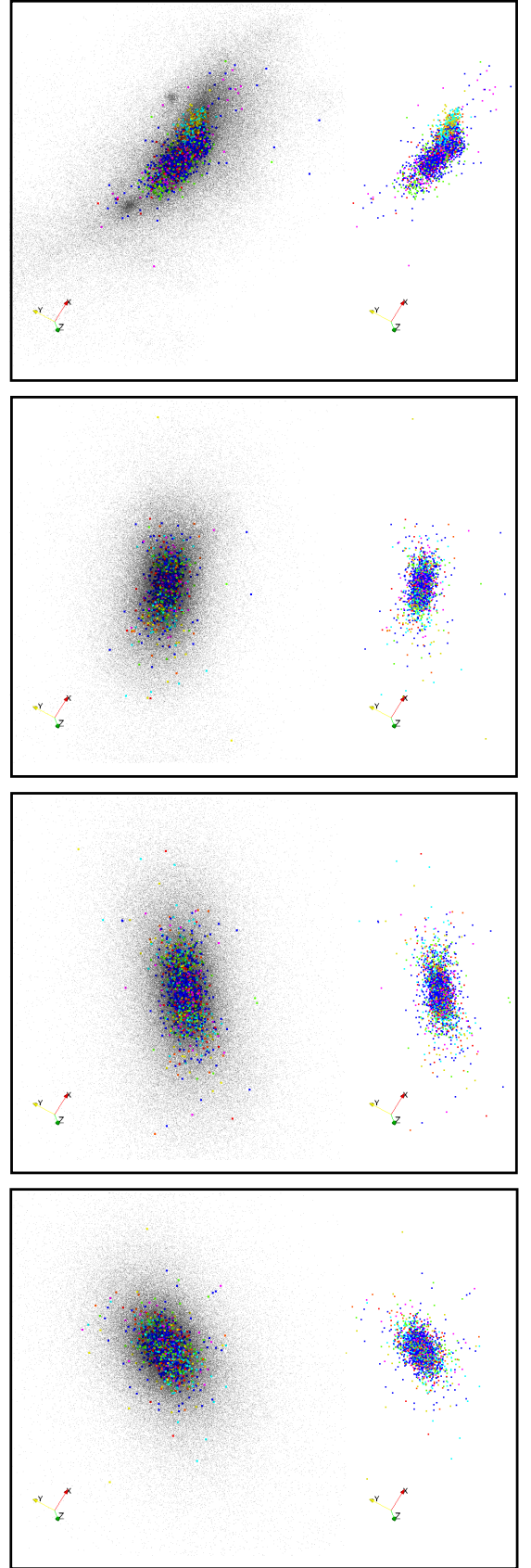


Figure 25. Same as Fig. 23 except the stages are $z = 24.1, 9.58, 3.82, 0$ or respectively $a = 0.040, 0.094, 0.21, 1.0$. In order to show subhaloes the plots are arbitrary zoomed in.

sidered various correlation properties of the flip-flop field estimated at fifty epochs and compared them with that of density and gravitational potential fields computed on the simulation particle by the GADGET code. We conclude that the flip-flop field $n_{\text{ff}}(\mathbf{q}, z)$ carries a wealth of information about the substructures in the collisionless Cosmic Web. In particular the peaks of the flip-flop field at the final stage $n_{\text{ff}}(\mathbf{q}, z = 0)$ store substantial information on the merging process.

The final flip-flop field looks like a set of bulky regions well isolated by narrow valleys, see Fig. 1, 2 and 4 for one-, two- and three-dimensional examples respectively. The peaks typically have a highly nested structure consisting of several smaller by sizes peaks which in turn may consist of even smaller peaks in Lagrangian space. The hierarchy can be very extensive and these properties are universal for collisionless self gravitating media in 1D, 2D and 3D. The topography of the flip-flop field is very different from a Gaussian field in all cases.

We selected a halo the central part of which has developed at least by $z \approx 10$ or even as early as $z \approx 20$ as Fig. 25 suggests. We used seven highest peaks in the flip-flop field $n_{\text{ff}}(\mathbf{q}, z = 0)$ within the largest peak in the simulation with 256^3 particles for a study of the robustness of the flip-flop field as an indicator of substructure existed in the halo. We demonstrated that the selected seven peaks were initially individual small haloes (Fig. 23) then they experienced multiple mergers (Fig. 24) and finally merged in a single approximately ellipsoidal cloud at the center of the halo (Fig. 25). During the following evolution from at least $z = 10$ or from even earlier epoch the merged seven peaks have remained at the center all the time. Although the orientation of the ellipsoid significantly changed but it remained intact until $z = 0$. It is remarkable that despite a very vigorous mixing in Eulerian configuration space and the lack of significant differences between mean and std velocities of the components the flip-flop field retains a 'record' of the merging tree in the form of easily identified isolated peaks, see Fig. 21 and 22.

The topography of the flip-flop landscape evolves rapidly after the onset of non-perturbative nonlinearity marked by the origin of the first regions with $n_{\text{ff}}(\mathbf{q}, z_{\text{nl}}) > 0$. However relatively soon its evolution is considerably impeded (see Fig. 12, 13 almost to complete freeze while the heights of peaks continue to grow. The latter indicates ongoing rapid dynamics inside the haloes and subhaloes themselves while the former suggests a remarkable stability of the flip-flop landscape.

We are suggesting the following explanation why only the flip-flop field has these unique characteristics. The period of time between sequential flip-flops of a fluid element is a characteristic time between its most significant dynamical metamorphoses. The dynamical significance of each flip-flop may be attributed to passing of the fluid element through the state of infinite density. Thus counting the flip-flops of a fluid element can be considered as counting ticks of its own dynamical clock. We demonstrated that there is a sort of dynamical instability: the greater the current counts of flip-flop the more likely the next one happens, see Fig. 14. This results in the remarkable stability of the topography of the flip-flop field, because the particles with lower counts of flip-flops have little chance to overtake their neighbors with

currently higher flip-flop counts. In other words it is very unlikely that the valleys of the flip-flop field will become peaks, see Fig. 2.

The flip-flop field approximates a very complicated structure of dark matter haloes and subhaloes in six-dimensional phase space as a much simpler set of tree-like structures in only four dimensions made by three Lagrangian axes and the number of flip-flops axis. Thus, the simplification is not only due to reduction of the number of dimensions but more importantly by the fact that the flip-flop distribution in Lagrangian space is a single valued function i.e. a field in three dimensions.

The discovered properties of the flip-flop field and easiness of its computing in cosmological N-body simulations make it a good candidate for a valuable addition to the suite of various techniques suggested for studies of substructures in the dark matter Cosmic Web. Neither density nor potential computed on particles by GADGET code possess such properties.

ACKNOWLEDGEMENTS

SSH acknowledges support by the Templeton Foundation and sabbatical support at Kapteyn Astronomical Institute at the University of Groningen The Netherlands and by Argonne National Labs where the significant part of the work was done. SSH also thanks S. Habib for fruitful discussions. The authors are grateful to S.D.M. White for useful critical comments on the first draft of the paper. MM acknowledges partial support by DOE and NSF via grants DE-FG02-07ER54940 and AST-1209665

REFERENCES

- Abel T., Hahn O., Kaehler R., 2012, *MNRAS*, **427**, 61
 Angulo R. E., Hahn O., Abel T., 2013, *MNRAS*, **434**, 3337
 Arnold V. I., Shandarin S. F., Zeldovich Y. B., 1982, *Geophysical and Astrophysical Fluid Dynamics*, **20**, 111
 Ascibar Y., Binney J., 2005, *MNRAS*, **356**, 872
 Cautun M., van de Weygaert R., Jones B. J. T., Frenk C. S., 2014, *MNRAS*, **441**, 2923
 Colberg J. M., et al., 2008, *MNRAS*, **387**, 933
 Couchman H. M. P., Carlberg R. G., 1992, *ApJ*, **389**, 453
 Davis M., Efstathiou G., Frenk C. S., White S. D. M., 1985, *ApJ*, **292**, 371
 Diemand J., Moore B., Stadel J., 2005, *Nature*, **433**, 389
 Ghigna S., Moore B., Governato F., Lake G., Quinn T., Stadel J., 1998, *MNRAS*, **300**, 146
 Gill S. P. D., Knebe A., Gibson B. K., 2004, *MNRAS*, **351**, 399
 Gurbatov S. N., Saichev A. I., Shandarin S. F., 1985, *Soviet Physics Doklady*, **30**, 921
 Gurbatov S. N., Saichev A. I., Shandarin S. F., 1989, *MNRAS*, **236**, 385
 Gurbatov S. N., Saichev A. I., Shandarin S. F., 2012, *Physics Uspekhi*, **55**, 223
 Hahn O., Angulo R. E., 2016, *MNRAS*, **455**, 1115
 Hidding J., van de Weygaert R., Vegter G., Jones B. J. T., Teillard M., 2012a, preprint, ([arXiv:1205.1669](https://arxiv.org/abs/1205.1669))
 Hidding J., van de Weygaert R., Vegter G., Jones B. J. T., 2012b, [arXiv](https://arxiv.org/abs/1211.5385), **1211.5385**, 1
 Hoffmann K., et al., 2014, *MNRAS*, **442**, 1197
 Klypin A., Gottlöber S., Kravtsov A. V., Khokhlov A. M., 1999, *ApJ*, **516**, 530

- Knebe A., et al., 2013, *MNRAS*, **435**, 1618
- Knollmann S. R., Knebe A., 2009, *ApJS*, **182**, 608
- Kofman L., Pogosyan D., Shandarin S. F., Melott A. L., 1992, *ApJ*, **393**, 437
- Landau L. D., Lifshitz E. M., 2008, *Mechanics. Course of Theoretical Physics v1*. Elsevier, Amsterdam
- Neyrinck M. C., 2012, *MNRAS*, **427**, 494
- Neyrinck M. C., Falck B. L., Szalay A. S., 2013, preprint, ([arXiv:1309.4787](https://arxiv.org/abs/1309.4787))
- Okamoto T., Habe A., 1999, *ApJ*, **516**, 591
- Ramachandra N. S., Shandarin S. F., 2015, *MNRAS*, **452**, 1643
- Ramachandra N. S., Shandarin S. F., 2016, preprint, ([arXiv:1608.05469](https://arxiv.org/abs/1608.05469))
- Schaap W. E., van de Weygaert R., 2000, *A&A*, **363**, L29
- Shandarin S. F., 1983, *Soviet Astronomy Letters*, **9**, 104
- Shandarin S. F., Medvedev M. V., 2014, preprint, ([arXiv:1409.7634](https://arxiv.org/abs/1409.7634))
- Shandarin S., Zeldovich Y., 1989, *Rev. Mod. Phys.*, **61**, 185
- Shandarin S., Habib S., Heitmann K., 2012, *Phys. Rev. D*, **85**, 083005
- Springel V., 2005, *MNRAS*, **364**, 1105
- Suginohara T., Suto Y., 1992, *ApJ*, **396**, 395
- Summers F. J., Davis M., Evrard A. E., 1995, *ApJ*, **454**, 1
- Vogelsberger M., White S. D. M., 2011, *MNRAS*, **413**, 1419
- Zel'dovich Y. B., 1970, *A&A*, **5**, 84
- Zeldovich Y. B., Einasto J., Shandarin S. F., 1982, *Nature*, **300**, 407
- van Kampen E., 1995, *MNRAS*, **273**, 295